A 14 h^{-3} Gpc³ study of cosmic homogeneity using BOSS DR12 quasar sample

Pierre Laurent,^a Jean-Marc Le Goff,^{a,1} Etienne Burtin,^a Jean-Christophe Hamilton,^b David W. Hogg,^c Adam Myers,^d Pierros Ntelis,^b Isabelle Pâris,^e James Rich,^a Eric Aubourg,^b Julian Bautista,^f Timothée Delubac,^g Hélion du Mas des Bourboux,^a Sarah Eftekharzadeh,^d Nathalie Palanque Delabrouille,^a Patrick Petitjean,^b Graziano Rossi,^{a,b} Donald P. Schneider,^{j,k} and Christophe Yeche^a

^aCEA, Centre de Saclay, IRFU/SPP, F-91191 Gif-sur-Yvette, France

^bAPC, Université Paris Diderot-Paris 7, CNRS/IN2P3, CEA, Observatoire de Paris, 10, rue A. Domon & L. Duquet, Paris, France

^cCenter for Cosmology and Particle Physics, New York University, 4 Washington Place, Meyer Hall of Physics, New York, NY 10003, USA

^dDepartment of Physics and Astronomy, University of Wyoming, Laramie, WY 82071, USA

^eAix Marseille UniversitÃl', CNRS, LAM (Laboratoire d'Astrophysique de Marseille) UMR 7326, 13388, Marseille, France

^fDepartment of Physics and Astronomy, University of Utah, Salt Lake City, UT 84112, USA.

^gLaboratoire d'astrophysique, Ecole Polytechnique Fédérale de Lausanne (EPFL), Observatoire de Sauverny, CH-1290 Versoix, Switzerland

^hInstitut d'Astrophysique de Paris, CNRS-UPMC, UMR7095, 98bis bd Arago, Paris, 75014 France

ⁱDepartment of Astronomy and Space Science, Sejong University, Seoul, 143-747, Korea

^jDepartment of Astronomy and Astrophysics, The Pennsylvania State University, University Park, PA 16802

^kInstitute for Gravitation and the Cosmos, The Pennsylvania State University, University Park, PA 16802

¹Corresponding author.

E-mail: jmlegoff@cea.fr

Abstract. The BOSS quasar sample is used to study cosmic homogeneity with a 3D survey over the largest volume used to date, $14 h^{-3} \text{ Gpc}^3$. The selected sample includes 47,858 quasars over 5983 deg² and in the range 2.2 < z < 2.8. We measure the count-in-sphere N(< r), i.e., the average number of objects around a given object, and its logarithmic derivative, the fractal correlation dimension $D_2(r)$. For a homogeneous distribution $N(< r) \propto r^3$ and $D_2(r) = 3$. With the simplest DD/RR estimator, these behaviors can be checked without determining an average density, which requires homogeneity to be defined. We observe the predicted behavior over one decade in the radius r. In particular, the fractal correlation dimension D_2 is found to be compatible with three on large scales at a high accuracy: $3 - \langle D_2 \rangle < 6 \times 10^{-4}$ (2 σ) over the range $250 < r < 1200 \, h^{-1} \text{Mpc}$. This result establishes homogeneity on large scales, therefore allowing us to define a reliable average density. We then introduce a more accurate estimator which requires a crude estimate of the average density, and find that the transition to homogeneity, described by N(< r) and $D_2(r)$, quantitatively agrees with the Λ CDM prediction and that D_2 is still compatible with three at an even higher accuracy: $3 - \langle D_2 \rangle < 1.5 \times 10^{-4}$ (2 σ) over the range $250 < r < 1200 \, h^{-1} \text{Mpc}$.

Keywords: Large scale structure of the universe, redshift surveys, galaxy clustering

C	Contents					
1	Introduction	2				
2	Observational sample	3				
	2.1 BOSS survey	3				
	2.2 Quasar selection	3				
3	Analysis	4				
	3.1 Survey completeness	4				
	3.2 Observables	6				
	3.3 Λ CDM prediction for $P(k)$, $\xi(r)$, $\mathcal{N}(\langle r)$ and $D_2(r)$	8				
	3.4 Covariance matrix	8				
4	Effects of systematics	10				
	4.1 Data-related effects	10				
	4.2 Analysis-related effects	12				
5	Results					
	5.1 Results with Peebles-Hauser estimator	14				
	5.2 Quasar bias	16				
	5.3 Results with the Landy-Szalay estimator	17				
6	Summary and discussion	19				
A	New estimator of $\mathcal{N}(< r)$	21				
В	B Dependance of estimators on average density					

1 Introduction

Modern cosmology relies on the assumption that the Universe is isotropic and homogeneous on large scales. Isotropy is well tested using the cosmic microwave background [1], the X-ray background [2] and the isotropy of radio galaxies [3]. The combination of isotropy and the Copernican principle, which states that we are not in a special location in the Universe, implies homogeneity according to Peacock [4] and Clarkson [5]. This conclusion, however, relies on the hypothesis of differentiability and therefore does not apply to fractal sets [6]. Indeed, Durrer et al. [7] provide an example of a fractal set which is isotropic as seen by an observer located anywhere on the fractal set. In this case the observer is not located in a special location and observes isotropy although the fractal set is not homogeneous.

In addition, the proof of homogeneity should not rely on just another principle. The Copernican principle was tested at the Gpc scale using the kinetic Sunyaev-Zel'dovich effect [8, 9] and spectral distortions of the cosmic-microwave-background (CMB) spectrum [10]. These results are sufficient to rule out models where we live in the center of a large (~ Gpc) void as an alternative to the existence of dark energy, but probably not to accurately guarantee homogeneity.

In brief, the cosmological principle is not enough to ensure homogeneity when combined with isotropy, and it is just another principle, not tested accurately enough. It is then highly desirable to directly test homogeneity and also to do it quantitatively, by measuring the transition to homogeneity from small scales to large scales and comparing it to model predictions.

This investigation has been performed with spectroscopic galaxy surveys, which provide a 3D map of the distribution of the galaxies. Some studies indeed found a transition to homogeneity at a scale between 70 and 150 h^{-1} Mpc [11–19], but other investigations failed to find this transition [20–25]. A definitive answer requires large and dense surveys with sufficiently simple geometry. The results obtained by the SDSS II [26] and WiggleZ [27] collaborations, which both found a transition to homogeneity, are therefore particularly relevant.

Galaxy surveys actually only measure density on our past light cone and not inside of it. Star formation history was used in an attempt to overcome this limitation and study homogeneity inside our past light cone [28]. Homogeneity was also positively tested using a combination of secondary CMB probes, including integrated Sachs-Wolfe, kinetic Sunyaev-Zel'dovich and Rees-Sciama effects, and CMB lensing [29]. These techniques allow homogeneity to be tested at much higher redshifts than galaxy surveys, up to recombination at $z \approx 1100$.

In this paper we use the quasar sample of the Baryon Oscillation Spectroscopic Survey (BOSS) [30] to study cosmic homogeneity with a 3D survey. This investigation is performed at high redshift, 2.2 < z < 2.8, and its volume of $14 h^{-3}$ Gpc³ is much larger than for previous studies: $0.25 h^{-3}$ Gpc³ for SDSS II [26] and $\sim 1 h^{-3}$ Gpc³ for WiggleZ [27]. A similar study is ongoing using the BOSS luminous-red-galaxy sample [31].

Quasars are rare objects and large enough samples to allow for detailed clustering studies [32–43] have only appeared recently. This paper presents the first study of cosmic homogeneity using a quasar sample.

We use Planck 2013 + WMAP9 parameters [44] as our fiducial flat Λ CDM cosmology, namely h=0.6704, $\Omega_m=0.3183$, $\Omega_b h^2=0.022032$, $n_s=0.9619$ and $\sigma_8=0.8347$. Throughout this paper, magnitudes use the asinh scale at low flux levels, as described by Lupton et al. [45]. The paper is organized as follows. Section 2 describes the quasar data sample used in this analysis, section 3 introduces the observables used to quantify the cosmic homogeneity and describes the analysis, section 4 discusses the effects of systematics, section 5 presents the results, and conclusions are drawn in section 6.

2 Observational sample

2.1 BOSS survey

The BOSS project of the Sloan Digital Sky Survey (SDSS-III) [46] was designed to obtain the spectra of over $\sim 1.6 \times 10^6$ luminous galaxies and $\sim 150,000$ quasars. The project uses upgraded versions of the SDSS spectrographs [47] mounted on the Sloan 2.5-meter telescope [48] at Apache Point Observatory, New Mexico.

An aluminum plate is set at the focal plane of the telescope with a 3° diameter field-of-view. Holes are drilled in the plate, corresponding to 1000 targets, i.e., objects to be observed with one of the two spectrographs. An optical fiber is plugged to each hole and sent to the spectrographs. The minimum distance between two fibers on the same plate corresponds to 62" on the sky, which results in some collisions between targets. It may, however, be possible to observe both colliding targets if they are in the overlap region between two or more plates.

The SDSS photometric images in 5 bands (u,g,r,i,z) [49] are used to define the targets. Selecting quasars in the redshift range $z \approx 2-3$ is difficult due to a background of objects with similar colors, namely metal-poor A and F stars, faint lower redshift quasars and compact galaxies [e.g., 50, 51]. In addition, BOSS operated close to the detection limits of the SDSS photometry, where uncertainties on flux measurements cause objects to scatter substantially in color space.

2.2 Quasar selection

The study of cosmic homogeneity requires a uniform selection across the sky, while BOSS is selecting quasars mainly for a Lyman- α Forest survey, which requires as many quasars as possible in a given redshift range but not necessarily with a uniform selection. The solution to reconcile these competing requirements was to define a CORE sample with uniform selection and a BONUS sample that aims at selecting as many quasars as possible using all information available in each patch of the sky. The CORE sample produces, on average, 20 targets per deg². In each plate, these CORE targets are completed with BONUS targets up to an allowed budget of 40 targets per deg². The CORE sample is selected using the extreme deconvolution (XD) algorithm, which is applied in BOSS to model the distributions of quasars and stars in flux space, and hence to separate quasar targets from stellar contaminants [XDQSO; 53].

In this paper, we consider as quasar targets all point sources in SDSS imaging up to the magnitude limit of BOSS quasar target selection, $g \le 22.0$ or $r \le 21.85$, that have an XDQSO probability above a threshold of 0.424 [54]. We use data from the final DR12 data release of SDSS-III [55]. Data are split into groups corresponding to a given version of the targeting algorithm, which are called chunks. During the first year of operation a different algorithm was used to define the CORE sample. Therefore some XDQSO targets are not included in our first-year sample and these data cannot easily be used to study homogeneity. This constraint removes all chunks up to chunk 11. For chunks 12 and 13, in case of collision, the CMASS galaxy targets had priority over the CORE targets [54]. Chunks 12 and 13 would require a special treatment involving masks around each galaxy target. Since our sample provides in any case a good statistical accuracy for the study of homogeneity, we prefer to limit ourselves to data that were taken in the same conditions and can be analyzed in a consistent manner. Removing these data, we are left with a small irregular patch of 1335 deg² in the South Galactic Cap (SGC). This patch is not optimal to study homogeneity, so we decided to remove all SGC data. Nevertheless, if we compute the fractal correlation dimension in the SGC, it is statistically compatible with that of the NGC, but with much larger error bars.

¹XD [52] is a method to describe the underlying distribution function of a series of points in parameter space (e.g., quasars in color space) by modeling that distribution as a sum of Gaussians convolved with measurement errors.

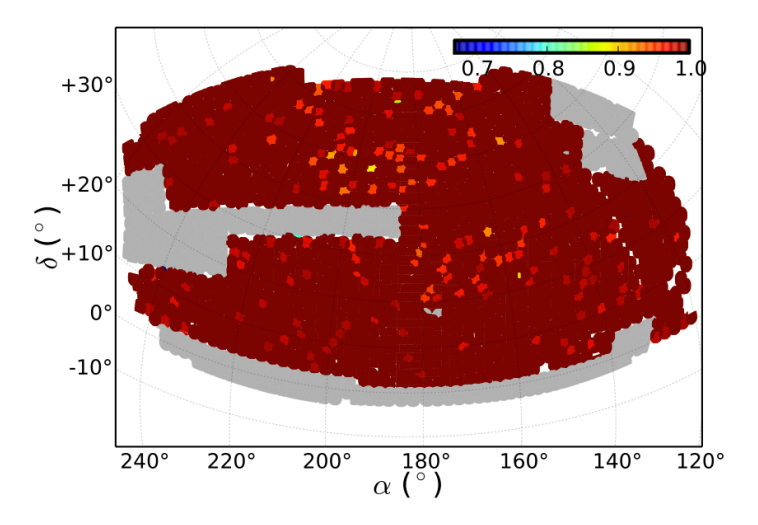


Figure 1. Angular distribution of the selected data (5983 deg²). The color scale indicates the survey completeness in each polygon. The grey area represents the full BOSS NGC footprint.

Our final sample consists of North Galactic Cap (NGC) data from chunks 14 and above. Figure 1 presents the resulting footprint, which covers 5983 deg² and includes 112,193 CORE targets. This footprint has an average of 20.2 targets per deg², out of which 13.9 actually have spectra consistent with them being a quasar. The BOSS pipeline [56] identifies all quasar targets and provides their redshifts. All spectra are then visually inspected [57, 58], to correct for misidentifications or inaccurate redshift determinations. The redshift is determined using the Mg II emission line if it is present in the spectrum, clearly detected, and not affected by sky subtraction. In other cases the redshift is estimated using the position of the red wing of the C IV emission line [57]. The uncertainty on the redshift determination is $\sigma_z \approx 0.001$ at one standard deviation.² Figure 2 presents the redshift distribution of the measured CORE targets. We limit the analysis to the range 2.2 < z < 2.8, where the distribution is significant. Table 1 lists some statistics on CORE targets.

3 Analysis

3.1 Survey completeness

The Mangle software [59–61] is used to define the geometry of the survey and to apply masks to remove bad areas. These bad areas include regions around bright stars and other bright objects, the center of each tile, which is covered by the centerpost of the cartridge, and bad photometric fields. This masking is done using polygons, which are defined as intersections of an arbitrary number of spherical caps on the celestial sphere.

In our sample, in case of fiber collision, the CORE targets have the highest priority. However, there are 772 CORE targets (0.7%), which could not be observed due to a collision with another CORE target. In these cases, we follow Anderson et al. [62] and assign a double weight to the colliding quasar that received a fiber. Since only 70% of the targets actually are quasars, the weight

² Pâris et al. [57] gives $\Delta z \approx 0.003$, but this is actually a 3 σ error.

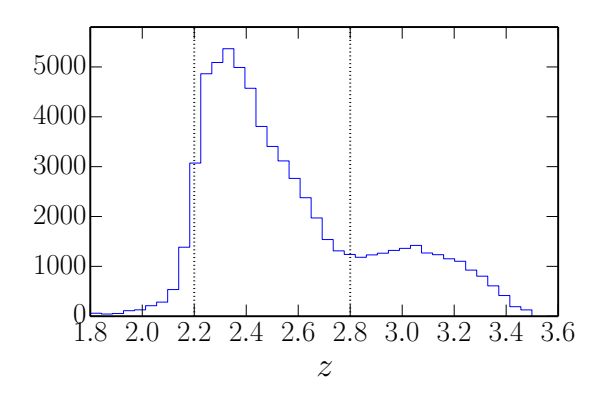


Figure 2. Redshift distribution of the measured CORE targets. The two vertical lines define the sample selected for the analysis (47,858 quasars out of 77,203).

should rather be smaller than two. But this is irrelevant to us since, after double weighting the colliding quasars, $\mathcal{N}(< r)$ varies around the uncorrected one with no particular trend and by less than half the statistical error on scales larger than 1 h^{-1} Mpc.

Fibers cannot be allocated to all targets due to the lack of available fibers on a given plate, and the targets that are not given a fiber are randomly selected. This effect is taken into account by defining a survey completeness,

$$C = \frac{N_{obs} + N_{coll}}{N_{target} - N_{known}} , (3.1)$$

in each polygon. Here N_{obs} is the number of targets that were allocated a fiber and then observed, N_{coll} is the number of targets that were not observed due to a collision with another target, N_{target} is the total number of targets and N_{known} refers to z < 2.15 quasar targets that had a spectrum measured previously and are not re-observed by BOSS. N_{known} only includes known quasars with z < 2.15 because known quasars at higher redshifts are re-observed by BOSS in order to improve the signal-to-noise ratio for the Lyman- α forest analysis. Therefore these quasars are treated as if they were not previously known. The position of the collided targets is correlated with the observed targets, so collisions are accounted for by upweighthing, as explained above, rather than completeness. Therefore N_{coll} is added to the numerator of the completeness.

Finally, N_{obs} includes objects with a spectrum but that failed to be identified or that could not be ascribed a redshift. These objects are very unlikely to be quasars, so they do not produce any loss in our sample and we do not make any correction for them. With the CORE plus BONUS strategy, there are only 249 not-collided CORE targets that were not allocated a fiber, as can be inferred from table 1. The completeness is unity in most polygons, as illustrated in figure 1, and the average completeness is 0.998.

As discussed in section 4, we apply a cut on the apparent *i*-band magnitude, $m_i < 21.3$, in order to mitigate the effects of systematics. In contrast with White et al. [63], we do not cut on the absolute magnitude. Our focus is not on defining a sample of quasars with the same properties, so we retain all to improve the statistics for the cosmic homogeneity study.

Targets in footprint	112,193
Targets with a fiber	111,172
Collisions between CORE	772
Quasars	77,203
2.2 < z < 2.8	47,858
$m_i < 21.3$	38,382

Table 1. Statistics of CORE targets.

3.2 Observables

In order to check for cosmic homogeneity it is important not to use a statistic that implicitly relies on the assumption of homogeneity. The evaluation of the correlation function, for instance, requires a mean density, which is only defined for a homogeneous sample. We use two related statistics, the counts-in-sphere N(< r), which is the average number of quasars in a sphere of radius r around a given quasar, and the fractal correlation dimension,

$$D_2(r) \equiv \frac{\mathrm{d} \ln N(\langle r)}{\mathrm{d} \ln r} \ . \tag{3.2}$$

If the distribution is homogeneous, then $N(< r) \propto r^3$ and $D_2(r) = 3$. If the distribution is fractal, D_2 is a measure of the fractal dimension. However, this statement is only true if the survey itself does not introduce inhomogeneities, which it actually does due to the survey geometry and the completeness. Following Scrimgeour et al. [27] we introduce N(< r), which is the ratio of N(< r) to the same quantity for a random homogeneous sample. This random sample is Poisson distributed on the sky with the same geometry and completeness as the measured quasars. It also has the same redshift distribution. For a homogeneous distribution, the scaled counts-in-sphere, N(< r), scales as r^0 and D_2 is now defined as

$$D_2(r) = \frac{\mathrm{d} \ln \mathcal{N}(< r)}{\mathrm{d} \ln r} + 3$$
 (3.3)

We use the *ransack* code from Mangle to generate a catalogue of 1,000,000 random objects over the selected footprint: the number of random objects generated in every polygon is directly proportional to its area times its completeness. The same masks, as applied to the data, are then applied to the random catalogue, which reduces the number of random objects to 950,000. This is 25 times the number of observed quasars in the same area. Since the statistical error declines as the square root of the number of pairs, the statistical error related to the random catalogue is 25 times smaller than that of the data, which is negligible. Each object in the catalogue is then assigned a redshift in the range 2.2 < z < 2.8 by drawing randomly according to the measured redshift distribution n(z). We are then insensitive to a possible isotropic variation of density with redshift, $\rho = \rho(r)$. This is a general issue for all 3D surveys, they cannot draw any conclusions, for example, about models where we live in the center of a spherical void.

Using the data and random catalogues, the following quantities are defined: DD(r) is the density of pairs of objects at a distance r, normalized to the total number of pairs, n(n-1)/2; RR(r) is the same quantity for the random catalogue and DR(r) is the normalized density of pairs with one data object and one random object. The random catalogue takes the completeness and geometry into account. However, the relative normalization of data and random catalogues implicitly depends on the assumed mean density.

The most straightforward estimator is

$$\hat{\mathcal{N}}^{\text{PH}}(< r) = \frac{\int_0^r DD(s) \, \mathrm{d}s}{\int_0^r RR(s) \, \mathrm{d}s} \,. \tag{3.4}$$

We define this expression as the Peebles-Hauser (PH) estimator of $\mathcal{N}(< r)$, similar to the Peebles and Hauser estimator [64] of the correlation function, $\hat{\xi}^{\text{PH}}(r) = DD/RR - 1$. The relative normalizations of DD and RR affects $\hat{\mathcal{N}}^{\text{PH}}(< r)$ only by a global normalization factor, which cancels exactly in the resulting $\hat{D}_2^{\text{PH}}(r)$. Therefore the PH estimator can be used to check that $\mathcal{N}(< r)$ reaches a constant value, or that $D_2(r)$ reaches 3, independently of any assumed mean density. It can be used to establish homogeneity. Alternatively, Scrimgeour et al. [27] uses $\int_0^r DD(s) \, ds / \int_0^r DR(s) \, ds$.

We also use a more sophisticated estimator, namely

$$\hat{N}^{LS}(< r) = 1 + \frac{\int_0^r \left[DD(s) - 2DR(s) + RR(s) \right] ds}{\int_0^r RR(s) ds} . \tag{3.5}$$

Appendix A explains how this estimator is obtained from the Landy and Szalay [65] optimal estimator of the correlation function, $\hat{\xi}^{LS}(r) = (DD - 2DR + RR)/RR$. We will therefore designate eq. 3.5 as the Landy-Szalay estimator for N(< r). In contrast with the simple PH estimator (eq. 3.4), this new estimator is not simply proportional to the relative normalizations of DD and RR. The dependence on the assumed mean density does not cancel exactly in the resulting $\hat{D}_2^{LS}(r)$. However, as discussed in appendix B, with this estimator a small relative error ϵ on the mean density results in a relative error on $\hat{N}^{LS}(< r)$ and $\hat{D}_2^{LS}(r)$ which is much smaller, $2\epsilon\xi + \epsilon^2$. Once homogeneity has been established using the simple PH estimator, we can define a mean density. The volume of the survey $(14 \ h^{-3} \ \text{Gpc}^3)$ is extremely large relative to the scale at which the Universe becomes homogeneous ($\sim 100 \ h^{-1} \ \text{Mpc}$, see figure 10). The mean density can therefore be accurately estimated from the data and the small remaining error, ϵ , will have a negligible effect on the new estimator.

In clustering studies, pairs of tracers are usually weighted according to the FKP weight [66] in order to improve the statistical accuracy: $w_{\text{FKP}} = 1/(1 + nP(k_0))$, where n is the tracer density and $P(k_0)$ is the power spectrum at the relevant scale k_0 . A scale of 40 h^{-1} Mpc corresponds to $k \approx 0.16$ h^{-1} Mpc. Our quasar sample is sparse, nP(k = 0.16) < 0.015 in all z bins, and the weight is always larger than 0.985. The relative gain on the statistical error, $\sqrt{1 + \sigma_w^2/\overline{w}^2}$, is on the order of 10^{-5} . The gain is even smaller at scales larger than $40 h^{-1}$ Mpc. This improvement is completely negligible and we do not use the FKP weight.

The measurements are performed using quasars, which are biased tracers of the underlying total matter distribution, with a bias b_Q . In order to evaluate $\mathcal{N}(< r)$ for the underlying matter distribution, the expression in eq. 3.4 and 3.5 must be corrected for bias:

$$\mathcal{N}(< r) - 1 = \frac{\mathcal{N}_Q(< r) - 1}{b_Q^2} \ . \tag{3.6}$$

Once $\mathcal{N}(< r)$ has been corrected for bias, the correlation dimension D_2 is calculated as in eq. 3.3. In the limit $|D_2 - 3| \ll 1$, eq. 3.6 gives

$$D_2(r) - 3 = \frac{D_{2Q}(r) - 3}{b_Q^2} \ . \tag{3.7}$$

The bias is measured by fitting the two-point correlation function of our sample, $\xi(r)$, with a Λ CDM model.

3.3 Λ CDM prediction for P(k), $\xi(r)$, $\mathcal{N}(\langle r)$ and $D_2(r)$

Since the distances to the quasars are obtained from their redshifts, the peculiar velocities of quasars along the lines of sight distort the measured distribution of quasars. This redshift-space distortion has two components which affect the matter power spectrum $P_m(k)$. On large scales, there is a linear effect arising from the infall of quasars towards local over-densities [67]. The resulting quasar power spectrum in redshift space is: $b_Q^2 (1 + \beta \mu^2)^2 P_m(k)$, where $\beta = f/b_Q$ and $f \approx \Omega_m^{0.55}(z)$ is the growth rate of structures [68]. At small scales (< 15 Mpc) we have the "finger-of-God" effect; the distortions become scale dependent and can be modeled using a *streaming* model [3]. This leads to:

$$P_{Q}(k,\mu) = b^{2} (1 + \beta \mu^{2})^{2} \frac{1}{1 + (k \sigma_{p} \mu)^{2}} P_{m}(k) , \qquad (3.8)$$

where σ_p is the pair-wise velocity dispersion along the line of sight. This velocity dispersion depends on the mass of the dark matter halos inhabited by the quasars. At our redshift, $z_{\rm eff}=2.39$, an average halo mass $\langle M \rangle \approx 2 \times 10^{12}\,M_{\odot}$ was inferred from the data using analytical models [43, 63, 69]. The MultiDark Run N-body simulations [70] indicate that the velocity dispersion for such haloes is $\sigma_p \approx 270\,{\rm km.s^{-1}}$. The error on the redshift measurement, $\sigma_z \approx 0.001$ (see end of section 2), is equivalent to an additional pair-wise velocity dispersion component of 125 km.s⁻¹. Adding the two components in quadrature leads to an expected value of $\sigma_p \approx 300\,{\rm km.s^{-1}}$.

The model for P(k) is transformed into a model for $\xi(r)$ using a Fast Fourier Transform (FFT) and the parameters of the model (bias and velocity dispersion) are fitted to the correlation function. We then have

$$\mathcal{N}(< r) = \frac{\int_0^r [1 + \xi(s)] s^2 \, \mathrm{d}s}{r^3 / 3}$$
 (3.9)

and $D_2(r)$ is found using eq. 3.3.

3.4 Covariance matrix

Since mock catalogues do not exist for the BOSS quasar sample, we use bootstrap resampling [71] to estimate the covariance matrix of $\xi(r)$, $\mathcal{N}(< r)$ and $D_2(r)$. We split our footprint into 201 cells with identical volumes. For each cell, we select 100 of the 200 other cells, and count the numbers of pairs DD, DR and RR. We include both pairs with the two quasars in the considered cell and pairs with one quasar in the considered cell and one quasar in one of the 100 selected cells. The selection of the 100 cells is done randomly but with the constraint that each pair of cells is selected exactly once. Drawing 201 cells with replacement out of the 201 cells provides a bootstrap realization. We sum the numbers of pairs DD, DR and RR for the 201 cells and compute the "measurements", $\xi(r)$, $\mathcal{N}(< r)$ and $D_2(r)$ for this realization. The covariance of the measurements for 1000 such bootstrap realizations provides an estimate of the covariance matrices.

The bootstrap procedure ignores cosmic variance, but this is not a serious problem in our case since, due to low density, shot noise strongly dominates. In addition there is a small correlation between the results in neighboring cells. This feature does not fit into the conditions of applicability of the bootstrap procedure, but this is a small effect.

Figure 3 presents the resulting correlation matrix for $\hat{\xi}^{LS}(r)$, $\hat{N}^{LS}(< r)$ and $\hat{D}_2^{LS}(r)$. The off-diagonal elements are quite small for $\hat{\xi}^{LS}(r)$, as expected for a shot-noise limited survey. A significant correlation is present for $\hat{N}^{LS}(< r)$ since $\int_0^r DD(s) \, ds$ is strongly correlated between two close values of r. The correlation is particularly large at large r. This result is not surprising, since at large r, due to the limited volume of the survey, the number of pairs does not increase as fast with r. The correlation matrix of $\hat{D}_2^{LS}(r)$ is strongly dominated by the diagonal, as for $\hat{\xi}^{LS}(r)$.

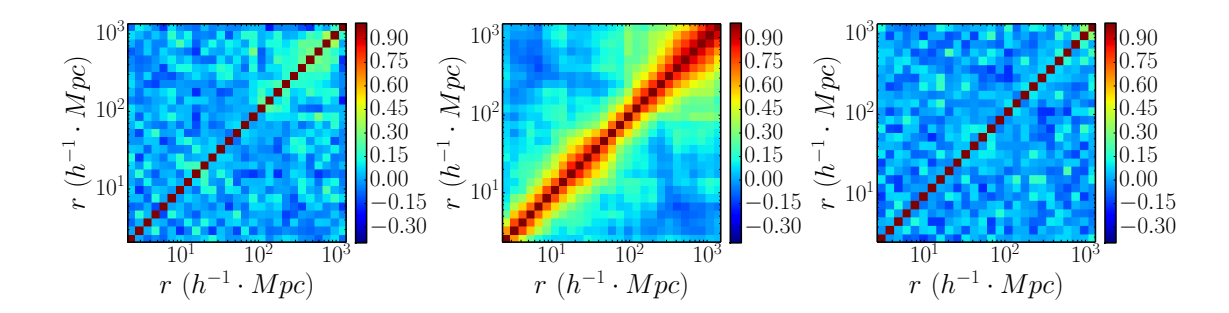


Figure 3. The correlation matrix of $\xi(r)$, $\mathcal{N}(< r)$ and $D_2(r)$ from left to right, with Landy-Szalay estimator. $D_2(r)$ is essentially uncorrelated. It is thus a more appropriate observable than $\mathcal{N}(< r)$, which is significantly correlated.

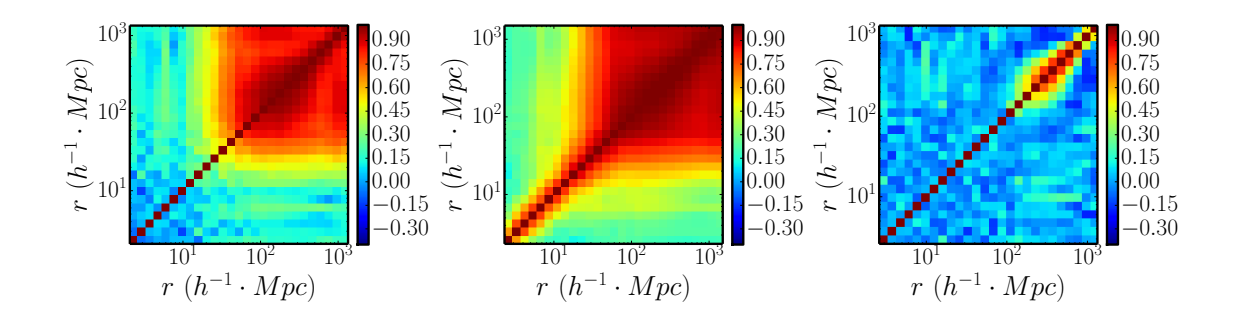


Figure 4. The correlation matrix of $\xi(r)$, $\mathcal{N}(< r)$ and $D_2(r)$ from left to right, with PH estimator (DD/RR). The observables are much more correlated with this estimator than with the Landy-Szalay estimator.

Figure 4 presents the correlation matrices obtained when using the simple PH estimator. In this case large non-diagonal elements are observed on large scales, both for $\hat{\xi}^{PH}(r)$ and $\hat{\mathcal{N}}^{PH}(< r)$. This feature is probably due to the definition of the estimator, where DD(r) and RR(r) are normalized to the total number of data and random pairs, respectively. The same global normalization was applied in all bootstrap cells. If instead we apply a different normalization in each cell, corresponding to the number of pairs in this cell, then the non-diagonal elements are significantly reduced. Appendix B demonstrates that an error in the normalization factor results in a constant error in $\hat{\xi}^{PH}(r)$. This error is different in each bootstrap cell, producing a constant contribution to the covariance matrix.³ At small r we have few pairs, the covariance matrix is large, the normalization contribution to the matrix is negligible, and the correlation remains nearly diagonal. In contrast, at large r, the normalization error dominates, it is completely correlated between r bins and the non-diagonal elements of the correlation matrix are close to unity. The normalization error cancels in the logarithmic derivative, $\hat{D}_2^{PH}(r)$, so that the correlation matrix of $\hat{D}_2^{PH}(r)$ is close to diagonal. Therefore, with the PH estimator, we will mostly consider the nearly uncorrelated $\hat{D}_2^{PH}(r)$ observable, which is easier to interpret. As explained in appendix B, in the case of the Landy-Szalay estimator, there is a cancellation between the effect of the normalization of DD, DR and RR. The estimator is insensitive at first order to the normalization

³The issue of normalization is inherent to the analysis. It is not an issue with bootstrap resampling and would also appear, e.g., with the jackknife method.

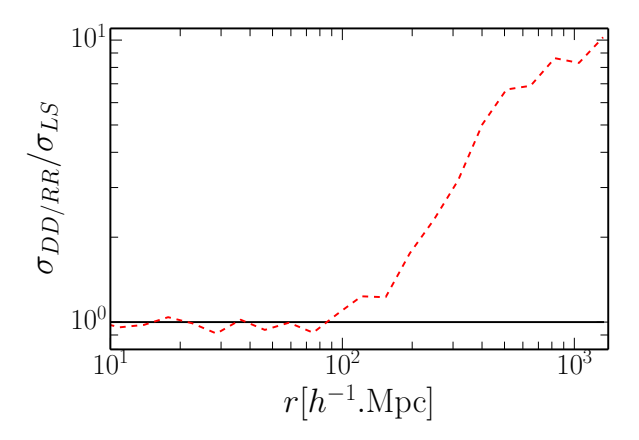


Figure 5. Ratio of the bootstrap error for PH estimator to LS estimator for $D_2(r)$. For $r > 100h^{-1}$ Mpc, there is a very significant gain in statistical accuracy with the LS estimator, up to a factor 10.

error and the correlation matrix of $\hat{\xi}^{LS}(r)$ remains nearly diagonal.

Varying the number of bootstrap cells from 25 to 201 does not change the general shape of the correlation matrices. It does, however, change individual elements of the diagonal of the covariance matrices by up to 20%, but there is no particular trend, and this simply illustrates the noisiness of the covariance estimator.

Figure 5 presents the ratio between the error for the PH estimator and the LS estimator. This ratio is estimated with the bootstrap procedure for the case of $D_2(r)$. There is probably a contribution to the error in addition to the Poisson error, present for the PH estimator and not for the LS estimator. On small scales the Poisson error dominates and the two estimators have the same error. On large scales there are many pairs, the Poisson error becomes small and there is a large gain with the LS estimator. This behavior is similar to what is described by Landy and Szalay [65] for $\hat{\xi}(\theta)$. The error ratio is even larger in the case of ξ and $\mathcal{N}(< r)$ due to the normalization error which cancels out in the Landy-Szalay estimator.

4 Effects of systematics

4.1 Data-related effects

Investigating homogeneity requires a homogeneous target selection, which is difficult to achieve in our redshift range, as explained in section 2. The dependence of target-selection completeness on redshift is accounted for by the use of a random catalogue in our estimators, at least in the limit that it is independent of angular position. But a dependence of the completeness with angular position will bias the measurement. This is the main source of systematics. Indeed, errors on the angular position of the quasars are negligible (of the order of kpc), and those on the redshift, $\sigma_z \approx 0.001$ at one standard deviation (i.e., $\approx 1 \ h^{-1}{\rm Mpc}$), were included in the model of the correlation function (see section 3.3). Finally, it was previously mentioned that there are few collisions and they have a negligible effect.

Quasar targets are selected in the SDSS photometric survey to a maximum limit $g \le 22$ or $r \le 21.85$ [54], while the average 5- σ detection-limits of the survey for point sources are g = 23.1 and r = 22.7. These detection limits vary with observational conditions such as seeing, airmass, Galactic extinction or sky brightness, by up to ± 0.8 magnitude. Some regions of the survey may

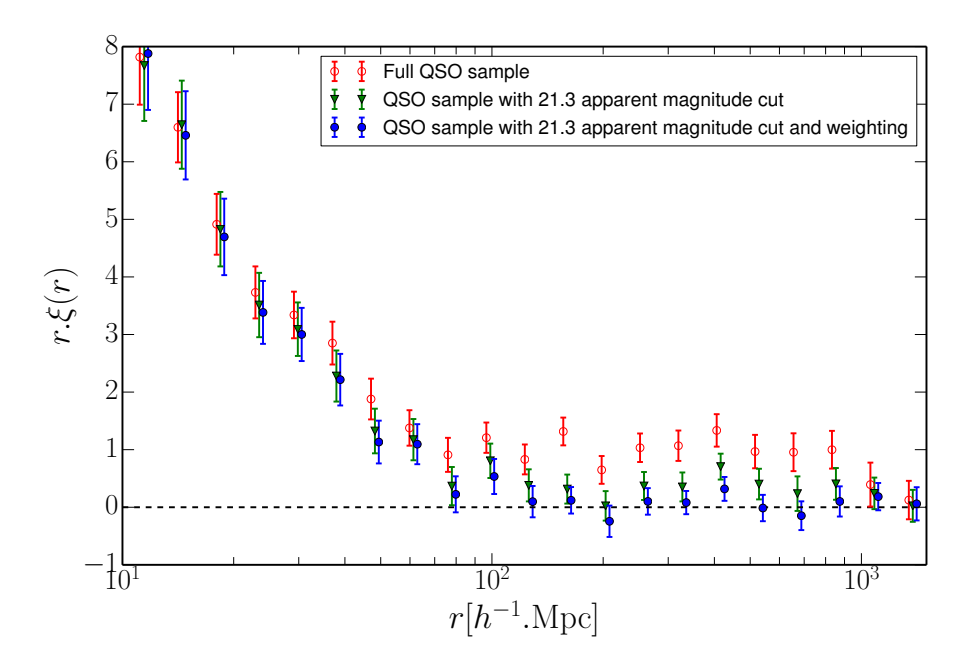


Figure 6. The function $r.\xi(r)$ obtained with the LS estimator for our quasar sample without cut (red open circles), after a 21.3 magnitude cut (green triangles) and after additional weighting (blue circles). The same blue points appear in the left panel of figure 11, where they can be compared to Λ CDM prediction.

then have targets with a magnitude just below the detection limit. Such targets have lower signal-to-noise ratio for their photometric fluxes and their intrinsic XDQSO probability is more likely to move below threshold. In addition faint quasars are more sensitive to blending, i.e., biases on their flux measurement due to the proximity of another object. We therefore exclude quasars with large apparent magnitudes. In order to be homogeneous, this procedure is done on magnitude that has been corrected for Galactic extinction. We chose to apply the cut in the *i* band since there are already limits in the target selection in the *g* and *r* bands. Starting from no cut and tightening the cut significantly changes the resulting correlation function, confirming that faint quasars are affected by the effects of systematics. When the threshold reaches $m_i = 21.3$, the correlation function stabilizes, providing a result less sensitive to systematics. This criterion reduces the sample by 20 %, as can be inferred from table 1. Figure 6 shows that the correlation function at large *r* is closer to zero after this cut. We obtain $\langle r, \xi(r) \rangle = 0.31 \pm 0.10$ over the range $120 < r < 1500 \ h^{-1}{\rm Mpc}$.

With this apparent magnitude cut set, we perform some simple checks on the analysis. We split our quasar sample in two subsamples of the same size, including quasars with seeing below or above the median seeing value in the r-band. The correlation functions for the two subsamples are found to be compatible. The same operation is performed with star density, airmass, Galactic extinction and sky brightness, leading to the same conclusion. One also must be aware of a possible systematic shift between redshifts obtained using different emission lines. In our redshift range, the MgII emission line is the most reliable line for fixing redshifts, although it is shifted to wavelengths that are beyond the BOSS coverage for redshifts above 2.5. As an additional check, we select quasars whose redshift is assigned with the MgII line and compute the correlation function for this subsample; the results are compatible with the correlation function for all quasars in the 2.2-2.5 redshift range.

Even after the apparent magnitude cut, targets remain closer to the detection limit in some parts of the sky, although with a safety margin. We therefore study whether the measured quasar density

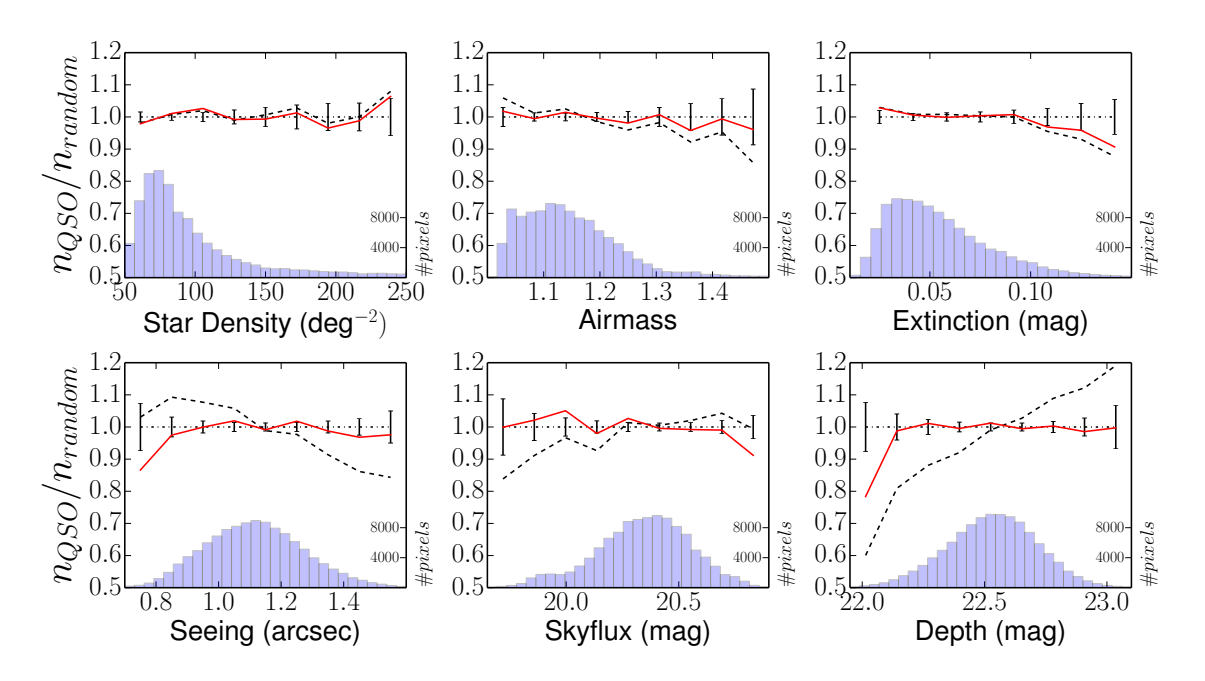


Figure 7. The n_{QSO}/n_{random} ratio versus star density, airmass, Galactic extinction, seeing, sky brightness (magnitude corresponding to the sky flux in 1 arcsec²) and survey depth (i.e., 5σ detection limit) in the i-band before (black dotted line) and after weighting depending on survey depth (continuous red line). The error bars are practically the same for the two curves. For sake of clarity the errors are drawn only once, on the line $n_{QSO}/n_{random} = 1$. The histograms show the distribution of the number of Healpix pixels for each quantity.

presents a dependence with respect to the 5- σ detection limit and to its inputs: the seeing, airmass, Galactic extinction and sky brightness. In addition, we consider the dependence with star density, since it influences the amplitude of blending effects. This procedure is similar to what was done in Ross et al. [72] for galaxy clustering. A HEALPix [73] map ($N_{side} = 256$) is produced for each quantity using SDSS photometric data, and also for the ratio of the number of measured quasars to the normalized number of randoms. The black lines in figure 7 show that this ratio varies significantly with all quantities except star density, suggesting that there is actually not much blending effect for our quasar sample.

The dependence with respect to the detection limit is independent of redshift and can be fitted with a straight line. This may be corrected by weighting the quasars in each pixel by the inverse of the value of the straight line fit corresponding to the 5- σ detection limit in the considered pixel. The red lines in figure 7 represent the new resulting $n_{\rm QSO}/n_{\rm random}$ ratios. The effects of systematics are then minimal. The blue points in figure 6 demonstrate that after applying this weighting, the correlation function at large r is consistent with zero. We find $\langle r.\xi(r)\rangle = 0.09 \pm 0.07$ over the range $120 < r < 1500 \ h^{-1}{\rm Mpc}$.

4.2 Analysis-related effects

In our determination of $\mathcal{N}(< r)$, we do not limit ourselves to spheres entirely included in the survey and we correct for the missing parts of the spheres by using random catalogues. In order to study whether this procedure can bias the measured $\mathcal{N}(< r)$ and $D_2(r)$, we generate fractal distributions over the survey geometry with a dimension below 3. We then send them through the analysis pipeline to check the reconstructed $\hat{D}_2(r)$.

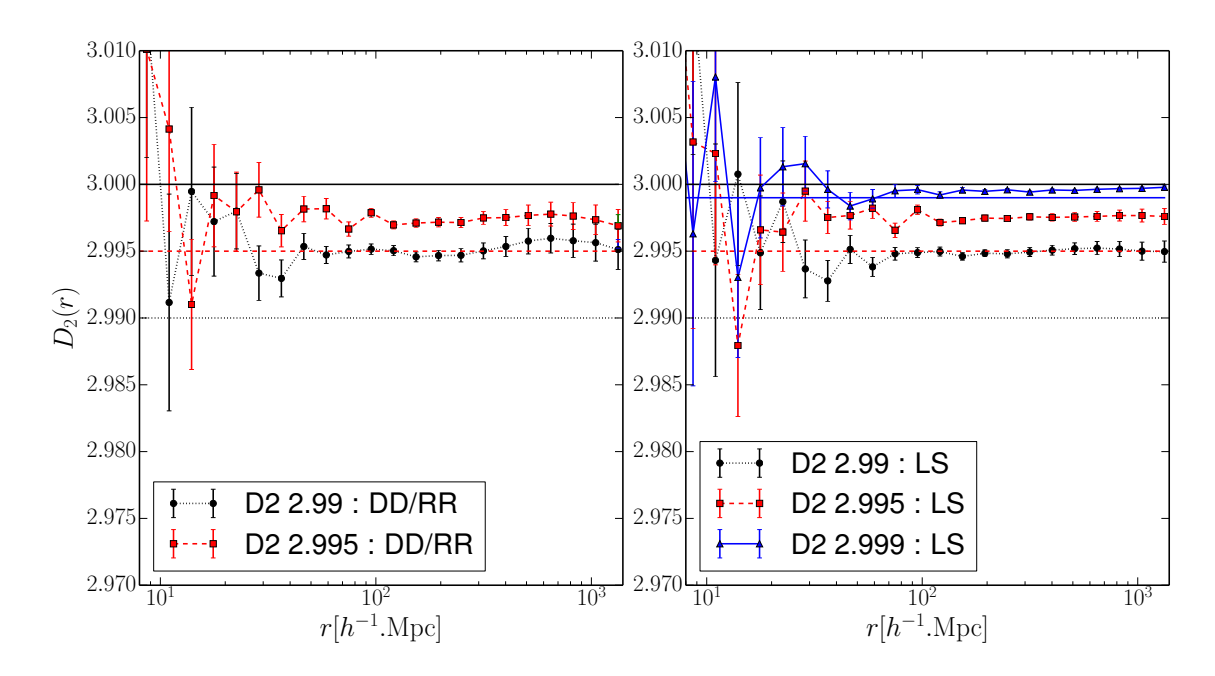


Figure 8. Reconstructed $D_2(r)$ averaged over 100 realizations for fractal distributions of various dimensions using PH (left) and LS (right) estimators. The reconstructed $D_2(r)$ appear typically twice as close to three as the real fractal dimensions of the sample indicated by horizontal lines.

In a first step, following Castagnoli & Provenzale [74], we create a cube embedding the full survey, with side $L = 36 h^{-1}$ Gpc. We divide this cube in M = 8 sub-cubes of side L/m with m = 2, and give to each sub-cube a survival probability p. We repeat this procedure for each surviving sub-cube, and so on. For an infinite number of iterations this provides a monofractal distribution with

$$D_2 = \frac{\log pM}{\log m} = 3 + \frac{\log p}{\log 2} \ . \tag{4.1}$$

This formula shows that using $p \le 1$ gives $D_2 \le 3$.

In a second step objects are drawn in the final sub-boxes. The number of objects in each sub-box is drawn using a Poisson distribution of mean $\lambda < 1$ and the position of the objects are randomly drawn in the sub-box. $\hat{D}_2(r)$ was computed for the resulting objects over the full $(36\ h^{-1}\ \text{Gpc})^3$ box using only spheres entirely included in the box. Eleven iterations in the first step were found to be enough to provide $\hat{D}_2(r)$ compatible with its expected value, even after averaging over 100 realizations of the full box.

Finally, the positions of the objects are converted from cartesian coordinates to observational coordinates RA, DEC and z. Cuts are applied to reproduce the footprint, masks, completeness and n(z) of the survey. The mean value of the Poisson distribution for the number of objects per sub-box is set so that the total number of objects after cuts matches the number of quasars in the real data. The resulting $\hat{D}_2(r)$ averaged over 100 realizations using the PH and LS estimators are shown in figure 8. They are significantly biased towards 3. The difference $3 - D_2$ is reduced by typically a factor 2, which is similar to what was observed by Scrimgeour et al. [27].

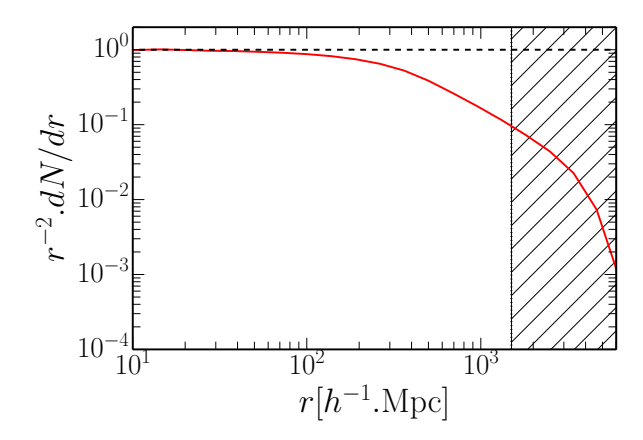


Figure 9. Density of pairs from the random catalogue separated by a distance r, divided by r^2 , $\frac{1}{r^2} \frac{dN}{dr}$, and normalized such that it is unity at small r. At large r this scaled density decreases due to the finite volume of the survey. For $r > 1500h^{-1}$ Mpc, it gets too low, and the hatched area is not included in the analysis.

5 Results

5.1 Results with Peebles-Hauser estimator

Figure 9 shows the density, dN/dr, of pairs from the random catalogue separated by a distance r, divided by r^2 . This scaled density is constant at small r and then decreases due to the finite volume of the survey. At $r = 1500 \ h^{-1}$ Mpc it is $\approx 10\%$ of its maximal value. The actual number of pairs in a bin of r is still increasing with r, so there is still information in N(< r) or N(< r). This is increasingly less the case for larger values of r and we decide to stop the analysis at $r = 1500 \ h^{-1}$ Mpc.

The green points in figure 10 are $\hat{N}^{\text{PH}}(< r)$ and $\hat{D}_2^{\text{PH}}(r)$ values obtained by using the simple PH estimator (eq. 3.4). We applied the masks and the magnitude cut, which are uncorrelated with the distribution of extragalactic quasars. We did not apply, however, the weighting depending on photometric survey depth. This weighting implies fitting the data to make the density flat with respect to the depth and it may bias the measurement towards homogeneity. Due to low quasar density, the measurement does not extend to very low values of r and the errors are significant at small r. However, for $6 < r < 25 \ h^{-1}\text{Mpc}$, the $\hat{N}^{\text{PH}}(< r)$ data are clearly compatible with a power law, $\hat{N}^{\text{PH}}(< r) \propto r^{-\gamma}$ with $\gamma = 0.60 \pm 0.03$, corresponding to a fractal correlation dimension, $D_2 = 2.40 \pm 0.03$. This result contrasts with the large scale regime ($r \gtrsim 100 \ h^{-1}\text{Mpc}$) where $\hat{N}^{\text{PH}}(< r)$ is found to be constant. With this estimator, N(< r) depends on the assumed average density only by a global normalization, so the fact that it is constant for $r \gtrsim 100 \ h^{-1}\text{Mpc}$ is independent of any assumption about an average density. Having $\hat{N}^{\text{PH}}(< r)$ constant over one decade in r indicates homogeneity.

However, as illustrated in figure 4, $\hat{N}^{\text{PH}}(< r)$ data points are highly correlated, making their interpretation difficult. It is therefore better to examine the $\hat{D}_2^{\text{PH}}(r)$ data points, which are not significantly correlated. With the PH estimator, the correlation dimension $D_2(r)$ is completely independent of any assumption about an average density and clearly reaches three at large r. Taking into account the covariance matrix, we get for the quasar distribution $3 - \langle D_2 \rangle = (-0.3 \pm 2.7) \times 10^{-3}$ (1 σ) over the range 250 $< r < 1200 \ h^{-1} \text{Mpc}$. This result corresponds to a 2σ upper limit of $3 - \langle D_2 \rangle < 5.1 \times 10^{-3}$. The quasar sample has an effective bias $b_Q = 4.25 \pm 0.14$. Correcting for

⁴This bias is obtained in section 5.2 using $\hat{\xi}^{LS}(r)$, which we can do since the measurement of $\hat{D}_2^{PH}(r)$ for quasars has established homogeneity and the possibility to measure the mean density.

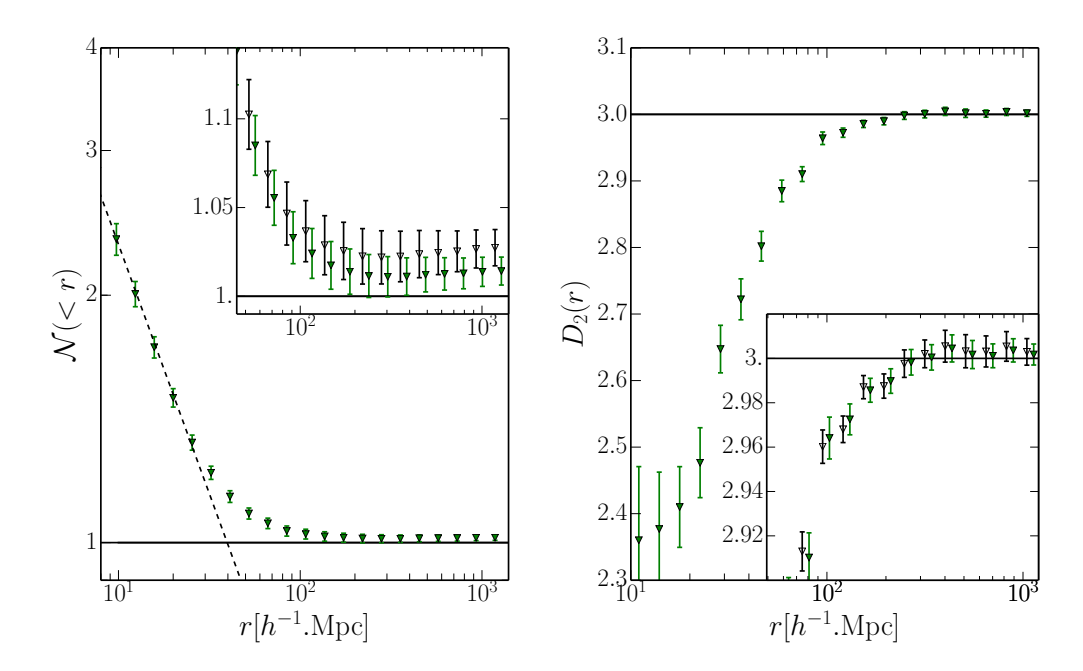


Figure 10. Scaled count-in-sphere N(< r) (left) and correlation dimension $D_2(r)$ (right) for the quasar sample as a function of the sphere radius r. These measurements are obtained with the simple PH estimator applying the masks and the magnitude cut (green triangles). The dashed line in the left panel is a power law fit for $6 < r < 25 h^{-1}$ Mpc. Each insert displays, in addition, the same observable without the mask and the magnitude cut (black open triangles). A constant N(< r) and $D_2(r)$ compatible with 3 establish homogeneity on large scales. The same conclusions apply with the green and black data points, so this result does not depend on analysis subtleties.

this bias gives $3 - \langle D_2 \rangle < 2.8 \times 10^{-4} \ (2 \ \sigma)$ for the matter distribution, over the range 250 < r < 1200 h^{-1} Mpc. This result clearly establishes homogeneity on large scales.

Section 4.2, however, shows that our estimator of D_2 is biased towards 3. The red points in the left panel of figure 8 indicate that, with the set of fractal distributions used, an input $3-D_2=5\times 10^{-3}$ gives a reconstructed $3-D_2=(2.56\pm0.11)\times 10^{-3}$ (averaged over the range 250< r<1200 $h^{-1}{\rm Mpc}$). This is a reduction by a factor 1.95 ± 0.08 . We therefore increase our upper limit by a factor 1.95+0.08=2.03 to get $3-\langle D_2\rangle<6\times 10^{-4}$ (2 σ) over the range 250< r<1200 $h^{-1}{\rm Mpc}$, for the matter distribution. This is the upper limit that we can set for such a set of fractal distributions. The reduction factor on $3-D_2$ might be larger for other sets of fractal distributions. Therefore, our upper limit applies only to the fractal distributions that we have studied. However, it seems reasonable to suppose that other fractal distributions would give similar reduction factors, and therefore similar limits.

The black points in figure 10 are $\hat{N}^{PH}(< r)$ and $\hat{D}_{2}^{PH}(r)$ values obtained without applying the masks and the apparent magnitude cut. They are similar to the green points, which suggests that our conclusions are quite robust and do not depend on analysis subtleties.

Sylos Labini [25] studied cosmic homogeneity using the main galaxy catalogue of SDSS DR7 [75]. In the range $5 < r < 20 \ h^{-1}$ Mpc, he found a power law index $\gamma = 0.88 \pm 0.05$, i.e., $D_2 = 2.12 \pm 0.05$. He also fit a power law in the region $30 < r < 150 \ h^{-1}$ Mpc, although this function does not perfectly fit his data, and found $\gamma = 0.2 \pm 0.05$, i.e., $D_2 = 2.8 \pm 0.05$. If we force a power law fit in this

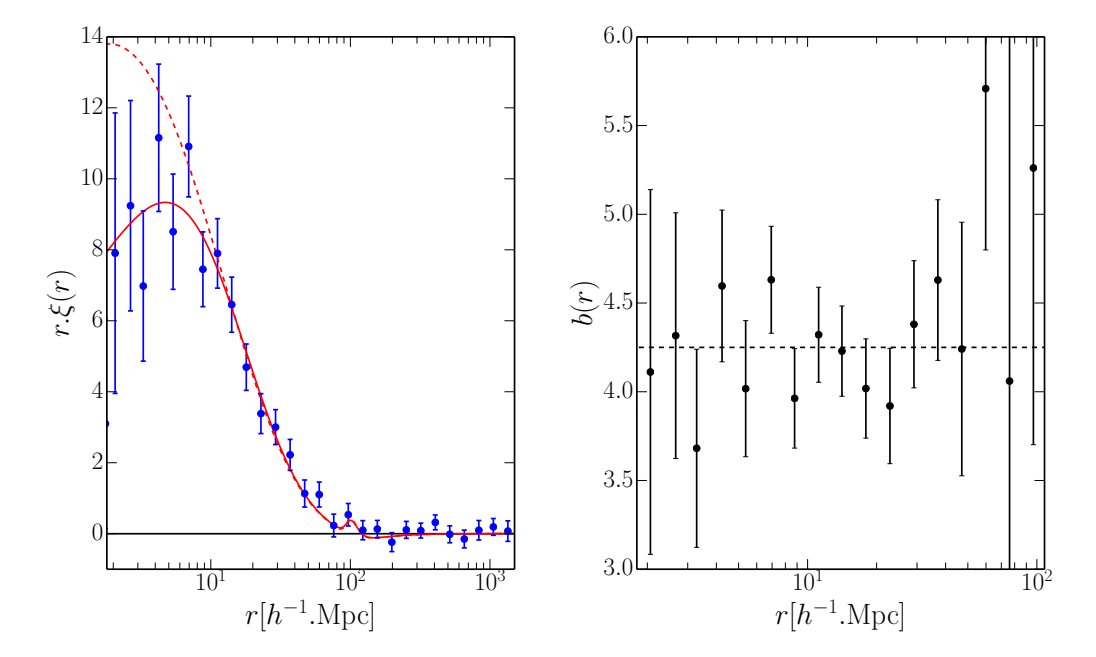


Figure 11. Left: the two-point correlation function of quasars in the BOSS sample as a function of their separation in redshift space. The dotted curve is the CAMB linear prediction (fitted over $10 < r < 85 \ h^{-1}$ Mpc) while the continuous curve is the nonlinear CAMB model with velocity dispersion (fitted over $2 < r < 85 \ h^{-1}$ Mpc). The continuous curve has $\chi^2 = 9$ for 16 degrees of freedom. The model is negative for $r > 120 \ h^{-1}$ Mpc but compatible with zero within the error of our data. Right: resulting quasar bias as a function of the separation r. The measured bias does not depend on the selected range in r.

 $30 < r < 150 \ h^{-1}$ Mpc range to our data, we find $\gamma = 0.109 \pm 0.012$. This result is also significantly different from zero, which is not a surprise since this is the region where we observe a transition to homogeneity. The two sets of data qualitatively agree with each other: fits to the data produce power laws with different non-zero indices below $r = 20 \ h^{-1}$ Mpc and for $30 < r < 150 \ h^{-1}$ Mpc, although the data are poor matches to the power law in the second range in r. The small level of discrepancy might be ascribed to the fact that the completeness of the survey and the masked regions are not taken into account in the Sylos Labini [25] analysis. This should affect $\mathcal{N}(< r)$ at some level because the completeness and the masks are not randomly distributed, and not accounting for them produces fake correlations. The important point is that the data used by Sylos Labini [25] do not extend to the region $r > 150 \ h^{-1}$ Mpc, where we clearly observe homogeneity.

The fact that $\hat{D}_2^{\text{PH}}(r) = 3$ over one decade in r at large scales establishes homogeneity, so that a mean density can be defined and, as discussed in section 3.2, we can use a more sophisticated and accurate estimator of $\mathcal{N}(< r)$, which requires at least a crude estimate of the average density (eq. 3.5). We now employ this estimator to accurately measure the quasar bias and to study the transition to homogeneity more accurately and compare it to Λ CDM prediction.

5.2 Quasar bias

We fit our measured 2-point correlation function, $\hat{\xi}^{LS}(r)$, with the model described in section 3.3, where we use Λ CDM prediction obtained with the CAMB program [76] for $P_m(k)$. The covariance of the data is obtained by bootstrap resampling, as discussed in section 3.4. As illustrated in figure 11

Zmin	z_{max}	Z_{eff}	b_Q	$\sigma_p ({\rm km \ s^{-1}})$	χ^2 (16 d.o.f.)
2.2	2.4	2.30	4.01 ± 0.22	757 ± 214	8
2.4	2.8	2.56	3.86 ± 0.19	314 ± 110	27
2.8	3.5	3.09	5.06 ± 0.83	708 ± 672	16
2.2	2.8	2.39	3.91 ± 0.14	416 ± 101	9

Table 2. Fit of bias over $2 < r < 85 h^{-1}$ Mpc in various redshift bins.

(left), we use two versions of the model, a linear CAMB prediction (dotted curve) with velocity dispersion set to zero, and a non-linear CAMB version provided by HALOFIT [77] with velocity dispersion (solid curve). There is a clear difference for scales below 15 h^{-1} Mpc, while the two predictions are in close agreement on larger scales. This difference arises mainly from the velocity dispersion and not HALOFIT. The non-linear fit with velocity dispersion perfectly describes the data. Fitting from $r=2\,h^{-1}$ Mpc up to $r=85\,h^{-1}$ Mpc, where the measured $\hat{\xi}^{\rm LS}(r)$ becomes compatible with zero, produces a bias $b_Q=3.91\pm0.14$, and a pair-wise velocity dispersion, $\sigma_p=416\pm101\,{\rm km.s^{-1}}$, with $\chi^2=9$ for 16 degrees of freedom. Figure 11 (right) shows that the bias is quite independent of the scale. Indeed, limiting the range of the fit to e.g. $2 < r < 42\,h^{-1}$ Mpc, hardly changes the result, $b_Q=3.87\pm0.14$. In addition, fitting with linear CAMB without velocity dispersion, but limiting the range of the fit to $10 < r < 42\,h^{-1}$ Mpc yields the same bias, $b_Q=3.87\pm0.14$. Therefore our estimation of the bias appears quite robust. Finally, table 2 shows the measured bias obtained in various redshift bins. One of the bins, 2.4 < z < 2.8, has a relatively poor χ^2 of 27 for 16 d.o.f., which has a probability of 4%.

The result of the fit for σ_p is in agreement with the estimation, $300 \, \mathrm{km.s^{-1}}$, obtained in section 3.3. The value of the quasar bias is in agreement with the fit $b_Q = 0.53 + 0.289 \, (1+z)^2$ by Croom et al. [34], which yields 3.85 at our average z = 2.39. There exist several other determinations of the quasar bias from BOSS data, namely $b_Q = 3.8 \pm 0.3$ from DR9 data [63], $b_Q = 3.54 \pm 0.11$ from DR12 data [69] and $b_Q = 3.64 \pm 0.15$ from the cross correlation of quasars and the Lyman- α Forest in DR9 [78]. Our value, 3.91 ± 0.14 , is slightly higher on average, but we include dispersion in our model of the correlation function, corresponding to eq. 3.8 for P(k), while these previous studies did not. They also limit the fit to a maximum $r \approx 25 \, h^{-1} \mathrm{Mpc}$. If we set $\sigma_p = 0$ in our model, we obtain $b_Q = 3.66 \pm 0.10$. If in addition we limit the fit to the range $2 < r < 26 \, h^{-1} \mathrm{Mpc}$, the result is $b_Q = 3.57 \pm 0.11$, in fair agreement with all other measurements from BOSS data.

In order to transform the $\mathcal{N}(< r)$ data for quasars to $\mathcal{N}(< r)$ for matter, using eq. 3.6, we need the effective bias, which includes the effect of linear redshift-space distortions. Fitting $\hat{\xi}^{\mathrm{LS}}(r)$ in the range $2 < r < 85 \ h^{-1}\mathrm{Mpc}$ with the model corresponding to eq. 3.8 with $b^2(1+\beta\mu^2)^2$ replaced by b_{eff}^2 , results in $b_{\mathrm{eff}}=4.25\pm0.14$. Alternatively, $\langle z\rangle=2.39$ produces $\Omega_m=0.947,\ f=0.970$ and $\beta=0.249$. Adopting the Kaiser formula [67], $b_{\mathrm{eff}}^2=(1+2\beta/3+\beta^2/5)b^2$, with b=3.91 yields $b_{\mathrm{eff}}=4.24$.

5.3 Results with the Landy-Szalay estimator

We now consider the more sophisticated estimator for $\mathcal{N}(< r)$ defined by eq. 3.5, similar to the Landy-Szalay estimator of the correlation function. We apply the masks, the magnitude cut and the weighting depending on survey depth. The effective bias and eq. 3.6 are used to correct the measurements and obtain $\hat{\mathcal{N}}^{LS}(< r)$ for the matter distribution, from which $\hat{D}_2^{LS}(r)$ is also obtained. We also apply eq. 3.6 to the model of section 3.3 to produce the corresponding Λ CDM predictions. Results are shown in Figure 12, where the transition to homogeneity is clearly visible. The region $r > 250 \ h^{-1}$ Mpc is expanded in Figure 13. The behaviors of $\mathcal{N}(< r)$ and $D_2(r)$ are accurately reproduced by the Λ CDM model (red curve). For $\mathcal{N}(< r)$ several adjacent points are above the curve, but the points are highly

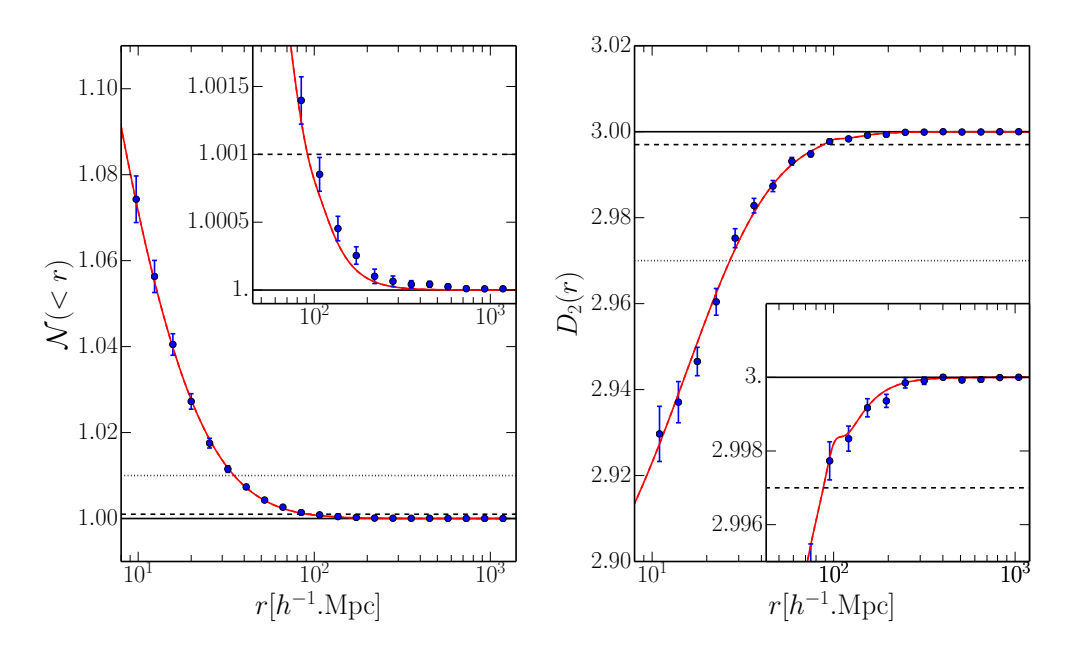


Figure 12. Scaled count-in-sphere N(< r) (left) and correlation dimension $D_2(r)$ (right) for the matter distribution as a function of the radius of the sphere r with LS estimator. The red curve is the Λ CDM model and the wiggle at $r \approx 100 \ h^{-1}$ Mpc in $D_2(r)$ is the BAO peak. The horizontal lines indicate the limits that define the one percent (dotted lines) and one per mil (dashed lines) homogeneity scales. The transition to homogeneity is accurately described by the Λ CDM model with $\chi^2 = 16$ and 12 for 18 degrees of freedom for N(< r) and $D_2(r)$, respectively.

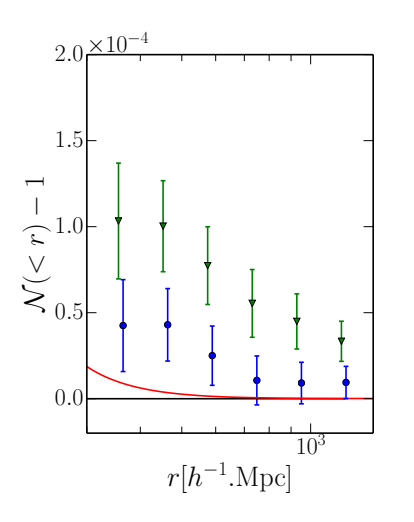
correlated in this region of r, as can be seen in figure 3. Indeed, when the full covariance is taken into account, we find $\chi^2 = 16$ for 18 degrees of freedom. A similar χ^2 is found for $D_2(r)$, 12 for 18 degrees of freedom.

In the region $250 < r < 1200 \ h^{-1}{\rm Mpc}$, we have $3 - \langle D_2 \rangle = (3.3 \pm 3.1) \times 10^{-4} \ (1 \ \sigma)$, which gives $3 - \langle D_2 \rangle < 9.4 \times 10^{-4} \ (2 \ \sigma)$ for the quasar distribution and $3 - \langle D_2 \rangle < 5.2 \times 10^{-5} \ (2 \ \sigma)$ for the matter distribution. As in section 5.1, we increase these upper limits to take into account the bias of the estimator towards 3. We get $3 - \langle D_2 \rangle < 1.5 \times 10^{-4} \ (2 \ \sigma)$ for the matter distribution.

Scrimgeour et al. [27] introduce two homogeneity scales, R_H . They are defined as the values of r for which $\mathcal{N}(< r)$ and $D_2(r)$ reach their nominal value within one percent, namely 1.01 for $\mathcal{N}(< r)$ and 2.97 for $D_2(r)$; they also define the values for 1 per mil. These thresholds are indicated in figure 12. Table 3 shows that our measurements of R_H are in good agreement with the values in our Λ CDM fiducial model.

However, our measurements of R_H depend on the value of the bias, which is obtained from the same data. Therefore, for R_H at 1 percent, the agreement is of moderate interest. Indeed, in this case $R_H < 40 \ h^{-1}$ Mpc, which is in the range of r where the bias is obtained by fitting $\xi(r)$. So the agreement just means that $\xi(r)$ can be fitted with a Λ CDM model up to $40 \ h^{-1}$ Mpc. The agreement at 1 per mil is more interesting. The bias is essentially obtained from the range $0 < r < 40 \ h^{-1}$ Mpc, higher r hardly contribute (see section 5.2). So the agreement means that using a bias measured on small scales, Λ CDM gives a good description of the transition to homogeneity around $100 \ h^{-1}$ Mpc.

In any case, the important result is the agreement of $\mathcal{N}(< r)$ and $D_2(r)$ with the fiducial ΛCDM



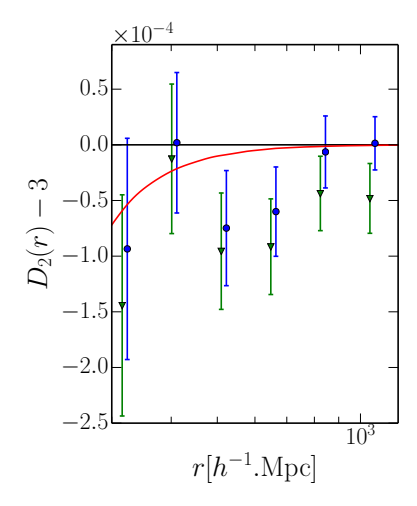


Figure 13. Expanded view of figure 12: N(< r) - 1 (left) and $D_2(r) - 3$ (right) for r > 300 h⁻¹Mpc. The red curve is the Λ CDM model. The green triangles are obtained from the quasar sample with apparent magnitude cut only, the blue circles are obtained with the weighted quasar sample. In this range of r, the N(< r) points are highly correlated. The right panel shows that $D_2(r)$ is statistically compatible with 3 at a high accuracy, indeed $\langle D_2 \rangle - 3 = (-1.8 \pm 1.7) \times 10^{-5}$ (1 σ).

	1 pei	rcent	1 per mil		
	$\hat{\mathcal{N}}^{\mathrm{LS}}(< r)$	$\hat{D}_2^{\mathrm{LS}}(r)$	$\hat{\mathcal{N}}^{\mathrm{LS}}(< r)$	$\hat{D}_2^{\mathrm{LS}}(r)$	
data	34.6 ± 1.2	26.2 ± 0.9	100 ± 7	88 ± 5	
ΛCDM	35.1	26.8	91.6	87.8	

Table 3. The homogeneity scale R_H in h^{-1} Mpc for $\mathcal{N}(< r)$ and $D_2(r)$ at 1 percent and 1 per mil.

model over a large range in r with only the bias as a free parameter (we still obtain a good agreement if we use the value of σ_p obtained in section 3.3 instead of fitting it to the data, and, in any case, σ_p is irrelevant for $r > 20 \ h^{-1}{\rm Mpc}$ for $\mathcal{N}(< r)$ and $30 \ h^{-1}{\rm Mpc}$ for $D_2(r)$).

Yadav et al. [79] define the homogeneity scale as the value of r for which the difference $3 - D_2(r)$ becomes smaller than the error on $D_2(r)$. They derive an upper limit of $\approx 260 \ h^{-1}$ Mpc for this homogeneity scale. This is quite consistent with our determination of $D_2(r)$ in figure 12, right. However, the upper limit is valid only in the limit of negligible shot noise, which is far from being our case. So this might just be a numerical coincidence.

6 Summary and discussion

The BOSS quasar sample in the range 2.2 < z < 2.8 was used to investigate cosmic homogeneity. The analysis was limited to 5983 deg² in order to mitigate systematic effects. These criteria provide a volume of $14 h^{-3}$ Gpc³, by far the largest volume ever used to study cosmic homogeneity with a 3D survey. These data allow a study of homogeneity up to a scale above $1 h^{-1}$ Gpc.

In order to mitigate systematic effects, we first apply masks based on Galactic objects and data acquisition, which should be uncorrelated with the distribution of extragalactic quasars. Faint quasars are more prone to systematics, indeed, they exhibit a different correlation function on large scales. We excise them, tightening the apparent magnitude cut until the correlation function is stable.

We do not use the correlation function to study homogeneity because its definition depends on the average density, which is only defined for a homogenous sample. We consider the counts-insphere N(< r), which is the average number of quasars in a sphere or radius r around a given quasar, and the fractal correlation dimension, which is its logarithmic derivative, $D_2(r) = d \ln N(< r)/d \ln r$. For a homogeneous sample $N(< r) \propto r^3$ and $D_2 = 3$.

Using the simplest PH estimator, the average density cancels out exactly in $D_2(r)$. Therefore, our finding that $3 - \langle D_2 \rangle < 2.8 \times 10^{-4}$ (2 σ) over the range 250 < r < 1200 h^{-1} Mpc clearly establishes homogeneity on large scales.

However, the distribution of the data is normalized to the distribution of a random catalogue, whose redshift distribution is taken from the data. This means that we are insensitive to a possible isotropic variation of density with redshift, $\rho = \rho(z)$. Our data do not exclude, for instance, models where we live at the center of a spherical void. We can test homogeneity up to a redshift dependence, or, in other words, check for isotropy in each slice in redshift. Although this issue is not much discussed in 3D survey publications, this is actually happening for any 3D survey of a given type of source. One cannot disentangle source evolution from variations of matter density with redshift. Indeed, Mustapha et al. [80] demonstrated that "if you fiddle the source evolution hard enough you can fit the observations to any FLRW model".

In order to convert measurements of angles and redshifts to physical distances (in Mpc) we need the angular distance $d_A(z)$ and the line-of-sight comoving distance $\chi(z)$. These are obtained assuming FLRW metrics, which rely on homogeneity, and the Λ CDM model. In our case, as we make no attempt to study evolution with redshift, the actual values of $d_A(z)$ and $\chi(z)$ are irrelevant. What we must assume is that these distances are independent of the direction on the sky. Strictly speaking, in the absence of inhomogeneous models to falsify, we are only performing a consistency check of the Λ CDM model. However, it is difficult to imagine an inhomogeneous Universe, resulting in $d_A(z)$ and $\chi(z)$ which depend on the direction on the sky in such a way as to compensate, in each slice in redshift, the inhomogeneities so as to make the object distributions appear isotropic in this slice in redshift.

Previous analyses by the SDSS II and WiggleZ collaborations also implied a homogeneous Universe, but the smaller volume of their samples did not allow them to reach large radii. The SDSS II analysis was limited to $r \approx 100~h^{-1}{\rm Mpc}$ and only saw the onset of homogeneity. The WiggleZ analysis reached $\approx 300~h^{-1}{\rm Mpc}$. Our analysis extends up to 1500 $h^{-1}{\rm Mpc}$. Such a large range unambiguously establish homogeneity. This result is at variance with another analysis of SDSS II data [25], but that analysis was limited to $r < 150~h^{-1}{\rm Mpc}$, so that it could only examine the transition region but not the large r region where homogeneity is clear.

Once homogeneity is established, we design a weighting scheme, based on the idea that average quasar density should not depend on the depth of the photometric survey. This results in a correlation function which is compatible with zero for separations larger than $100\ h^{-1}{\rm Mpc}$. Karagiannis et al. [81] also measured the correlation function of the BOSS quasar sample on large scales, reporting it to be non-zero, and interpreted this result as an indication of primordial non-Gaussianities, which we do not confirm. We ascribe the discrepancy to the fact that they used the DR9 sample, a period during which the definition of the CORE sample was not stable, and they did not apply the same cuts and weighting as we did to mitigate the effects of systematics.

We measure a quasar bias $b_Q = 3.91 \pm 0.14$. This result appears quite robust, and is in particular insensitive to the range of the fit. We have shown that small discrepancies between our result and earlier determinations of the quasar bias from BOSS data [63, 69, 78] result simply from model choices.

We also introduce a more sophisticated estimator, similar to the Landy Szalay estimator [65]

for $\xi(r)$. With this estimator the average density does not cancel out exactly in $D_2(r)$, but once we have a reasonable estimate of the density, the relative error in $\mathcal{N}(< r)$ and $D_2(r)$ is proportional to the square of the relative error in the average density. The analysis with the PH estimator has established homogeneity to high precision, and the volume of the survey is large compared to the homogeneity scale. We thus have a fair estimate of the mean density, and the resulting error in $\mathcal{N}(< r)$ and $D_2(r)$ with the new estimator is negligible. In addition, this new estimator is more accurate than the PH estimator, by up to a factor 10 on the largest scales. We use this new estimator to quantitatively study the transition to homogeneity, which is found to agree with the predictions of Λ CDM. The fractal correlation dimension D_2 is found to be compatible with 3 at a high accuracy: $(3 - D_2) < 5.2 \times 10^{-5}$ (at 1 σ) over the range $250 < r < 1200 \ h^{-1}$ Mpc.

In our determination of $\mathcal{N}(< r)$, we do not limit ourselves to spheres entirely included in the survey and we correct for missing parts of the spheres by using random catalogues. When this procedure is applied to a set of simulated fractal distributions, the resulting D_2 appears to be biased towards 3, i.e. $3 - D_2$ is reduced by typically a factor 2. So for such a set of fractal distributions the upper limits have to be increased to $3-D_2 < 6 \times 10^{-4}$ for the PH estimator and to $3-D_2 < 1.5 \times 10^{-4}$ for the LS estimator. The reduction factor on $3 - D_2$ might be larger for others set of fractal distributions. So, strictly speaking, we cannot set an upper limit on $3 - D_2$ that is valid for any fractal distribution. It seems, however, reasonable to assume that a similar upper limit will be obtained if the reduction factor on $3 - D_2$ is computed for another set of fractal distributions. The fact is that we are not aware of any cosmological fractal model to be tested and possibly falsified.

A New estimator of $\mathcal{N}(< r)$

If $\tilde{N}(s)$ is the number of pairs for a homogeneous sample, the Landy Szalay estimator of the correlation function is

$$1 + \hat{\xi}^{LS}(s) = \frac{N(s)}{\tilde{N}(s)} = 1 + \frac{DD(s) - 2DR(s) + RR(s)}{RR(s)}$$
(A.1)

and

$$\mathcal{N}(< r) = \frac{N(< r)}{\tilde{N}(< r)} = \frac{\int_0^r \frac{N(s)}{\tilde{N}(s)} \tilde{N}(s) \, \mathrm{d}s}{\int_0^r \tilde{N}(s) \, \mathrm{d}s} = 1 + \frac{\int_0^r [DD(s) - 2DR(s) + RR(s)] \, \mathrm{d}s}{\int_0^r RR(s) \, \mathrm{d}s} , \qquad (A.2)$$

where we used RR(s) as an estimator of $\tilde{N}(s)$.

B Dependance of estimators on average density

The *DD*, *DR* and *RR* pair counts in the estimators are normalized to $n_d(n_d-1)/2$, $n_d \times n_r$ and $n_r(n_r-1)/2$, respectively. This normalization assumes that the average density of the Universe is given by the average density of our sample. The key point is the relative density of data and random, so we can ascribe the error on the average density to the data and not the random. We will assume that the error on the average density is of order ϵ , which results in a factor $(1 + \epsilon)^2$ on DD and $(1 + \epsilon)$ on DR, and no error on *RR*. With the PH estimator, the effect on $\xi(r)$ is

$$\Delta \hat{\xi}^{\text{PH}} = \left(\frac{DD(1+\epsilon)^2}{RR} - 1\right) - \left(\frac{DD}{RR} - 1\right) = 2\epsilon \frac{DD}{RR} + \epsilon^2 \frac{DD}{RR} = (2\epsilon + \epsilon^2)(1+\xi) \approx 2\epsilon , \qquad (B.1)$$

since $\xi \ll 1$ and $\epsilon \ll 1$. This result is a constant independent of r and introduces a constant factor $1 + 2\epsilon$ on $\mathcal{N}(\langle r)$.

With the Landy-Szalay estimator

$$\Delta \hat{\xi}^{LS} = \left(\frac{DD(1+\epsilon)^2 - 2DR(1+\epsilon) + RR}{RR}\right) - \left(\frac{DD - 2DR + RR}{RR}\right) = 2\epsilon \frac{DD - DR}{RR} + \epsilon^2 \frac{DD}{RR}$$
$$= 2\epsilon \xi + \epsilon^2 (1+\xi) \approx 2\epsilon \xi + \epsilon^2 , \tag{B.2}$$

where (DD - DR)/RR is the Hewett [82] estimator of ξ . Since $\xi \ll 1$ and $\epsilon \ll 1$, the effect is much smaller than the 2ϵ effect with the PH estimator.

Acknowledgments

We thank Jean-Philippe Uzan, Cyril Pitrou and Ruth Durrer for useful discussions.

Funding for SDSS-III has been provided by the Alfred P. Sloan Foundation, the Participating Institutions, the National Science Foundation, and the U.S. Department of Energy Office of Science. The SDSS-III web site is http://www.sdss3.org/.

SDSS-III is managed by the Astrophysical Research Consortium for the Participating Institutions of the SDSS-III Collaboration including the University of Arizona, the Brazilian Participation Group, Brookhaven National Laboratory, Carnegie Mellon University, University of Florida, the French Participation Group, the German Participation Group, Harvard University, the Instituto de Astrofisica de Canarias, the Michigan State/Notre Dame/JINA Participation Group, Johns Hopkins University, Lawrence Berkeley National Laboratory, Max Planck Institute for Astrophysics, Max Planck Institute for Extraterrestrial Physics, New Mexico State University, New York University, Ohio State University, Pennsylvania State University, University of Portsmouth, Princeton University, the Spanish Participation Group, University of Tokyo, University of Utah, Vanderbilt University, University of Virginia, University of Washington, and Yale University.

References

- [1] Smoot, G. F., C. L. Bennett, A. Kogut, et al. Structure in the COBE differential microwave radiometer first-year maps. *Astrophys. J. Lett.*, 396:L1–L5, 1992.
- [2] Scharf, C. A., K. Jahoda, M. Treyer, et al. The 2-10 keV X-Ray Background Dipole and Its Cosmological Implications. *Astrophys. J.*, 544:49–62, 2000. astro-ph/9908187.
- [3] Peebles, P. J. E. *The large-scale structure of the universe*. Research supported by the National Science Foundation. Princeton, N.J., Princeton University Press, 1980. 435 p., 1980.
- [4] Peacock, J. A. Cosmological Physics. Cosmological Physics, by John A. Peacock, pp. 704. ISBN 052141072X. Cambridge, UK: Cambridge University Press, January 1999., 1999.
- [5] Clarkson, C. Establishing homogeneity of the universe in the shadow of dark energy. *Comptes Rendus Physique*, 13:682–718, 2012. arXiv:1204.5505.
- [6] Durrer, R. . private communication, 2015.
- [7] Durrer, R., J.-P. Eckmann, F. Sylos Labini, et al. Angular projections of fractal sets. *EPL (Europhysics Letters)*, 40:491–496, 1997. astro-ph/9702116.
- [8] Stebbins, A. CMB Spectral Distortions from the Scattering of Temperature Anisotropies. *ArXiv Astrophysics e-prints*, 2007. astro-ph/0703541.
- [9] Caldwell, R. R. and A. Stebbins. A Test of the Copernican Principle. *Physical Review Letters*, 100: 191302, 2008. arXiv:0711.3459.

- [10] Zhang, P. and A. Stebbins. Confirmation of the Copernican Principle at Gpc Radial Scale and above from the Kinetic Sunyaev-Zel'dovich Effect Power Spectrum. *Physical Review Letters*, 107:041301, 2011. arXiv:1009.3967.
- [11] Martinez, V. J. and P. Coles. Correlations and scaling in the QDOT redshift survey. *Astrophys. J.*, 437: 550–555, 1994.
- [12] Guzzo, L. Is the universe homogeneous? (On large scales). *New Astron.*, 2:517–532, 1997. astro-ph/9711206.
- [13] Martinez, V. J., M.-J. Pons-Borderia, R. A. Moyeed, et al. Searching for the scale of homogeneity. *Mon. Not. Roy. Astron. Soc.*, 298:1212–1222, 1998. astro-ph/9804073.
- [14] Scaramella, R., L. Guzzo, G. Zamorani, et al. The ESO Slice Project [ESP] galaxy redshift survey. V. Evidence for a D=3 sample dimensionality. *Astron. and Astrophys.*, 334:404–408, 1998. astro-ph/9803022.
- [15] Amendola, L. and E. Palladino. The Scale of Homogeneity in the Las Campanas Redshift Survey. *Astrophys. J. Lett.*, 514:L1–L4, 1999. astro-ph/9901420.
- [16] Pan, J. and P. Coles. Large-scale cosmic homogeneity from a multifractal analysis of the PSCz catalogue. *Mon. Not. Roy. Astron. Soc.*, 318:L51–L54, 2000. astro-ph/0008240.
- [17] Kurokawa, T., M. Morikawa, and H. Mouri. Scaling analysis of galaxy distribution in the Las Campanas Redshift Survey data. *Astron. and Astrophys.*, 370:358–364, 2001.
- [18] Yadav, J., S. Bharadwaj, B. Pandey, et al. Testing homogeneity on large scales in the Sloan Digital Sky Survey Data Release One. *Mon. Not. Roy. Astron. Soc.*, 364:601–606, 2005. astro-ph/0504315.
- [19] Sarkar, P., J. Yadav, B. Pandey, et al. The scale of homogeneity of the galaxy distribution in SDSS DR6. *Mon. Not. Roy. Astron. Soc.*, 399:L128–L131, 2009. arXiv:0906.3431.
- [20] Coleman, P. H. and L. Pietronero. The fractal structure of the universe. *Phys. Rep.*, 213:311–389, 1992.
- [21] Pietronero, L. and F. Montuori, M.and Sylos Labini. *Critical Dialogues in Cosmology*. World Scientific Press, Singapore, 1997.
- [22] Sylos Labini, F., M. Montuori, and L. Pietronero. Scale-invariance of galaxy clustering. *Phys. Rep.*, 293:61–226, 1998. astro-ph/9711073.
- [23] Joyce, M., M. Montuori, and F. S. Labini. Fractal Correlations in the CFA2-South Redshift Survey. *Astrophys. J. Lett.*, 514:L5–L8, 1999. astro-ph/9901290.
- [24] Sylos Labini, F., N. L. Vasilyev, and Y. V. Baryshev. Breaking the self-averaging properties of spatial galaxy fluctuations in the Sloan Digital Sky Survey Data release six. *Astron. and Astrophys.*, 508: 17–43, 2009. arXiv:0909.0132.
- [25] Sylos Labini, F. Very large-scale correlations in the galaxy distribution. *EPL (Europhysics Letters)*, 96: 59001, 2011. arXiv:1110.4041.
- [26] Hogg, D. W., D. J. Eisenstein, M. R. Blanton, et al. Cosmic Homogeneity Demonstrated with Luminous Red Galaxies. *Astrophys. J.*, 624:54–58, 2005. astro-ph/0411197.
- [27] Scrimgeour, M. I., T. Davis, C. Blake, et al. The WiggleZ Dark Energy Survey: the transition to large-scale cosmic homogeneity. *Mon. Not. Roy. Astron. Soc.*, 425:116–134, 2012. arXiv:1205.6812.
- [28] Hoyle, B., R. Tojeiro, R. Jimenez, et al. Testing Homogeneity with Galaxy Star Formation Histories. *Astrophys. J. Lett.*, 762:L9, 2013. arXiv:1209.6181.
- [29] Zibin, J. P. and A. Moss. Nowhere to hide: closing in on cosmological homogeneity. *ArXiv e-prints*, 2014. arXiv:1409.3831.
- [30] Dawson, K. S., D. J. Schlegel, C. P. Ahn, et al. The Baryon Oscillation Spectroscopic Survey of SDSS-III. *Astronom. J.*, 145:10, 2013. arXiv:1208.0022.

- [31] Ntelis, P., J.-C. Hamilton, E. Burtin, et al. Exploring cosmic homogeneity with the BOSS DR12 Galaxy sample. *to be published*, 2016.
- [32] Croom, S. M., T. Shanks, B. J. Boyle, et al. The 2dF QSO Redshift Survey II. Structure and evolution at high redshift. *Mon. Not. Roy. Astron. Soc.*, 325:483–496, 2001. astro-ph/0012375.
- [33] Porciani, C., M. Magliocchetti, and P. Norberg. Cosmic evolution of quasar clustering: implications for the host haloes. *Mon. Not. Roy. Astron. Soc.*, 355:1010–1030, 2004. astro-ph/0406036.
- [34] Croom, S. M., B. J. Boyle, T. Shanks, et al. The 2dF QSO Redshift Survey XIV. Structure and evolution from the two-point correlation function. *Mon. Not. Roy. Astron. Soc.*, 356:415–438, 2005. astro-ph/0409314.
- [35] Hennawi, J. F., M. A. Strauss, M. Oguri, et al. Binary Quasars in the Sloan Digital Sky Survey: Evidence for Excess Clustering on Small Scales. *Astronom. J.*, 131:1–23, 2006. astro-ph/0504535.
- [36] Myers, A. D., R. J. Brunner, G. T. Richards, et al. First Measurement of the Clustering Evolution of Photometrically Classified Quasars. *Astrophys. J.*, 638:622–634, 2006. astro-ph/0510371.
- [37] Porciani, C. and P. Norberg. Luminosity- and redshift-dependent quasar clustering. *Mon. Not. Roy. Astron. Soc.*, 371:1824–1834, 2006. astro-ph/0607348.
- [38] Myers, A. D., R. J. Brunner, R. C. Nichol, et al. Clustering Analyses of 300,000 Photometrically Classified Quasars. I. Luminosity and Redshift Evolution in Quasar Bias. *Astrophys. J.*, 658:85–98, 2007. astro-ph/0612190.
- [39] Myers, A. D., R. J. Brunner, G. T. Richards, et al. Clustering Analyses of 300,000 Photometrically Classified Quasars. II. The Excess on Very Small Scales. *Astrophys. J.*, 658:99–106, 2007. astro-ph/0612191.
- [40] da Ângela, J., T. Shanks, S. M. Croom, et al. The 2dF-SDSS LRG and QSO survey: QSO clustering and the L-z degeneracy. *Mon. Not. Roy. Astron. Soc.*, 383:565–580, 2008. astro-ph/0612401.
- [41] Croom, S. M., G. T. Richards, T. Shanks, et al. The 2dF-SDSS LRG and QSO Survey: the spectroscopic QSO catalogue. *Mon. Not. Roy. Astron. Soc.*, 392:19–44, 2009. arXiv:0810.4955.
- [42] Shen, Y., M. A. Strauss, N. P. Ross, et al. Quasar Clustering from SDSS DR5: Dependences on Physical Properties. *Astrophys. J.*, 697:1656–1673, 2009. arXiv:0810.4144.
- [43] Ross, N. P., Y. Shen, M. A. Strauss, et al. Clustering of Low-redshift ($z \le 2.2$) Quasars from the Sloan Digital Sky Survey. *Astrophys. J.*, 697:1634–1655, 2009. arXiv:0903.3230.
- [44] Planck Collaboration, P. A. R. Ade, N. Aghanim, et al. Planck 2013 results. XVI. Cosmological parameters. *Astron. and Astrophys.*, 571:A16, 2014. arXiv:1303.5076.
- [45] Lupton, R. H., J. E. Gunn, and A. S. Szalay. A Modified Magnitude System that Produces Well-Behaved Magnitudes, Colors, and Errors Even for Low Signal-to-Noise Ratio Measurements. *Astronom. J.*, 118:1406–1410, 1999. astro-ph/9903081.
- [46] Eisenstein, D. J., D. H. Weinberg, E. Agol, et al. SDSS-III: Massive Spectroscopic Surveys of the Distant Universe, the Milky Way, and Extra-Solar Planetary Systems. *Astronom. J.*, 142:72, 2011. arXiv:1101.1529.
- [47] Smee, S. A., J. E. Gunn, A. Uomoto, et al. The Multi-object, Fiber-fed Spectrographs for the Sloan Digital Sky Survey and the Baryon Oscillation Spectroscopic Survey. *Astronom. J.*, 146:32, 2013. arXiv:1208.2233.
- [48] Gunn, J. E., W. A. Siegmund, E. J. Mannery, et al. The 2.5 m Telescope of the Sloan Digital Sky Survey. *Astronom. J.*, 131:2332–2359, 2006. astro-ph/0602326.
- [49] Fukugita, M., T. Ichikawa, J. E. Gunn, et al. The Sloan Digital Sky Survey Photometric System. *Astronom. J.*, 111:1748, 1996.
- [50] Fan, X. Simulation of Stellar Objects in SDSS Color Space. *Astronom. J.*, 117:2528–2551, 1999. astro-ph/9902063.

- [51] Richards, G. T., X. Fan, D. P. Schneider, et al. Colors of 2625 Quasars at 0 < z < 5 Measured in the Sloan Digital Sky Survey Photometric System. *Astronom. J.*, 121:2308–2330, 2001. astro-ph/0012449.
- [52] Bovy, J., D. W. Hogg, and S. T. Roweis. Extreme deconvolution: Inferring complete distribution functions from noisy, heterogeneous and incomplete observations. *AOAS*, 5:1657, 2009. arXiv:0905.2979.
- [53] Bovy, J., J. F. Hennawi, D. W. Hogg, et al. Think Outside the Color Box: Probabilistic Target Selection and the SDSS-XDQSO Quasar Targeting Catalog. *Astrophys. J.*, 729:141, 2011. arXiv:1011.6392.
- [54] Ross, N. P., A. D. Myers, E. S. Sheldon, et al. The SDSS-III Baryon Oscillation Spectroscopic Survey: Quasar Target Selection for Data Release Nine. *Astrophys. J. Suppl.*, 199:3, 2012. arXiv:1105.0606.
- [55] Alam, S., F. D. Albareti, C. Allende Prieto, et al. The Eleventh and Twelfth Data Releases of the Sloan Digital Sky Survey: Final Data from SDSS-III. *ArXiv e-prints*, 2015. arXiv:1501.00963.
- [56] Bolton, A. S., D. J. Schlegel, É. Aubourg, et al. Spectral Classification and Redshift Measurement for the SDSS-III Baryon Oscillation Spectroscopic Survey. *Astronom. J.*, 144:144, 2012. arXiv:1207.7326.
- [57] Pâris, I., P. Petitjean, É. Aubourg, et al. The Sloan Digital Sky Survey quasar catalog: ninth data release. *Astron. and Astrophys.*, 548:A66, 2012. arXiv:1210.5166.
- [58] Pâris, I., P. Petitjean, É. Aubourg, et al. The Sloan Digital Sky Survey quasar catalog: tenth data release. *Astron. and Astrophys.*, 563:A54, 2014. arXiv:1311.4870.
- [59] Blanton, M. R., H. Lin, R. H. Lupton, et al. An Efficient Targeting Strategy for Multiobject Spectrograph Surveys: the Sloan Digital Sky Survey "Tiling" Algorithm. *Astronom. J.*, 125:2276–2286, 2003. astro-ph/0105535.
- [60] Tegmark, M., M. R. Blanton, M. A. Strauss, et al. The Three-Dimensional Power Spectrum of Galaxies from the Sloan Digital Sky Survey. *Astrophys. J.*, 606:702–740, 2004. astro-ph/0310725.
- [61] Swanson, M. E. C., M. Tegmark, A. J. S. Hamilton, et al. Methods for rapidly processing angular masks of next-generation galaxy surveys. *Mon. Not. Roy. Astron. Soc.*, 387:1391–1402, 2008. arXiv:0711.4352.
- [62] Anderson, L., E. Aubourg, S. Bailey, et al. The clustering of galaxies in the SDSS-III Baryon Oscillation Spectroscopic Survey: baryon acoustic oscillations in the Data Release 9 spectroscopic galaxy sample. *Mon. Not. Roy. Astron. Soc.*, 427:3435–3467, 2012. arXiv:1203.6594.
- [63] White, M., A. D. Myers, N. P. Ross, et al. The clustering of intermediate-redshift quasars as measured by the Baryon Oscillation Spectroscopic Survey. *Mon. Not. Roy. Astron. Soc.*, 424:933–950, 2012. arXiv:1203.5306.
- [64] Peebles, P. J. E. and M. G. Hauser. Statistical Analysis of Catalogs of Extragalactic Objects. III. The Shane-Wirtanen and Zwicky Catalogs. *Astrophys. J. Suppl.*, 28:19, 1974.
- [65] Landy, S. D. and A. S. Szalay. Bias and variance of angular correlation functions. *Astrophys. J.*, 412: 64–71, 1993.
- [66] Feldman, H. A., N. Kaiser, and J. A. Peacock. Power-spectrum analysis of three-dimensional redshift surveys. *Astrophys. J.*, 426:23–37, 1994. astro-ph/9304022.
- [67] Kaiser, N. Clustering in real space and in redshift space. Mon. Not. Roy. Astron. Soc., 227:1–21, 1987.
- [68] Linder, E. V. and R. N. Cahn. Parameterized beyond-Einstein growth. *Astroparticle Physics*, 28: 481–488, 2007. astro-ph/0701317.
- [69] Eftekharzadeh, S., A. D. Myers, M. White, et al. Clustering of intermediate redshift quasars using the final SDSS III-BOSS sample. *ArXiv e-prints*, 2015. arXiv:1507.08380.
- [70] Prada, F., A. A. Klypin, A. J. Cuesta, et al. Halo concentrations in the standard Λ cold dark matter cosmology. *Mon. Not. Roy. Astron. Soc.*, 423:3018–3030, 2012. arXiv:1104.5130.

- [71] Efron, B. and G. Gong. A Leisurely Look at the Bootstrap, the Jackknife, and Cross-Validation. *The American Statistician*, page 37, 1983.
- [72] Ross, A. J., W. J. Percival, A. G. Sánchez, et al. The clustering of galaxies in the SDSS-III Baryon Oscillation Spectroscopic Survey: analysis of potential systematics. *Mon. Not. Roy. Astron. Soc.*, 424: 564–590, 2012. arXiv:1203.6499.
- [73] Górski, K. M., E. Hivon, A. J. Banday, et al. HEALPix: A Framework for High-Resolution Discretization and Fast Analysis of Data Distributed on the Sphere. *Astrophys. J.*, 622:759–771, 2005. astro-ph/0409513.
- [74] Castagnoli, C. and A. Provenzale. From small-scale fractality to large-scale homogeneity A family of cascading models for the distribution of galaxies. *Astron. and Astrophys.*, 246:634–643, 1991.
- [75] Abazajian, K. N., J. K. Adelman-McCarthy, M. A. Agüeros, et al. The Seventh Data Release of the Sloan Digital Sky Survey. *Astrophys. J. Suppl.*, 182:543–558, 2009. arXiv:0812.0649.
- [76] Lewis, A., A. Challinor, and A. Lasenby. Efficient Computation of Cosmic Microwave Background Anisotropies in Closed Friedmann-Robertson-Walker Models. *Astrophys. J.*, 538:473–476, 2000. astro-ph/9911177.
- [77] Smith, R. E., J. A. Peacock, A. Jenkins, et al. Stable clustering, the halo model and non-linear cosmological power spectra. *Mon. Not. Roy. Astron. Soc.*, 341:1311–1332, 2003. astro-ph/0207664.
- [78] Font-Ribera, A., E. Arnau, J. Miralda-Escudé, et al. The large-scale quasar-Lyman α forest cross-correlation from BOSS. *JCAP*, 5:18, 2013. arXiv:1303.1937.
- [79] Yadav, J. K., J. S. Bagla, and N. Khandai. Fractal dimension as a measure of the scale of homogeneity. *Mon. Not. Roy. Astron. Soc.*, 405:2009–2015, 2010. arXiv:1001.0617.
- [80] Mustapha, N., C. Hellaby, and G. F. R. Ellis. Large-scale inhomogeneity versus source evolution Can we distinguish them observationally? *Mon. Not. Roy. Astron. Soc.*, 292:817, 1997. gr-qc/9808079.
- [81] Karagiannis, D., T. Shanks, and N. P. Ross. Search for primordial non-Gaussianity in the quasars of SDSS-III BOSS DR9. *Mon. Not. Roy. Astron. Soc.*, 441:486–502, 2014. arXiv:1310.6716.
- [82] Hewett, P. C. The estimation of galaxy angular correlation functions. *Mon. Not. Roy. Astron. Soc.*, 201: 867–883, 1982.